



Published in final edited form as:

Sci Signal. ; 12(583): . doi:10.1126/scisignal.aaw9450.

KRAS^{G12C} inhibition produces a driver-limited state revealing collateral dependencies

Kevin Lou¹, Veronica Steri^{2,3}, Alex Y. Ge^{2,4}, Y. Christina Hwang^{2,5}, Christopher H. Yagodinski^{2,4}, Arielle R. Shkedi⁶, Alex L. M. Choi^{2,5}, Dominique C. Mitchell^{2,5}, Danielle L. Swaney^{1,7}, Byron Hann^{2,3}, John D. Gordan^{2,5}, Kevan M. Shokat^{1,8,*}, Luke A. Gilbert^{2,4,9,*}

¹Department of Cellular and Molecular Pharmacology, University of California, San Francisco, San Francisco, CA 94158, USA.

²Helen Diller Family Comprehensive Cancer Center, University of California, San Francisco, San Francisco, CA 94158, USA.

³Preclinical Therapeutics Core, University of California, San Francisco, San Francisco, CA 94158, USA.

⁴Department of Urology, University of California, San Francisco, San Francisco, CA 94158, USA

⁵Department of Medicine and Division of Hematology/Oncology, University of California, San Francisco, San Francisco, CA 94158, USA

⁶Institute for Neurodegenerative Diseases and Department of Pharmaceutical Chemistry, University of California San Francisco, San Francisco 94158, CA, USA

⁷Quantitative Biosciences Institute (QBI), University of California, San Francisco, San Francisco, CA 94158, USA.

⁸Howard Hughes Medical Institute, University of California, San Francisco, San Francisco, CA 94143, USA.

⁹Innovative Genomics Institute, University of California, San Francisco, San Francisco, CA 94158, USA

Abstract

Inhibitors targeting KRAS^{G12C}, a mutant form of the guanosine triphosphatase (GTPase) KRAS, are a promising new class of oncogene-specific therapeutics for the treatment of tumors driven by the mutant protein. These inhibitors react with the mutant cysteine residue by binding covalently

*Corresponding author. luke.gilbert@ucsf.edu (L.A.G.); kevan.shokat@ucsf.edu (K.M.S.).

Author contributions: K.L., J.D.G., K.M.S., and L.A.G. were responsible for the conception, design, and interpretation of the experiments and wrote the manuscript. K.L., V.S., A.Y.G., Y.C.H., C.H.Y., A.R.S., A.L.M.C., D.C.M., D.L.S., B.H., and L.A.G. performed experiments, interpreted data, and read or edited the manuscript.

Competing interests: Kin of K.L. hold stock in and are employed by Pharmaron, a contract research organization. K.M.S. is an inventor on a UC Regents–owned patent application covering KRAS^{G12C} inhibitors, which has been licensed to Araxes Pharma LLC. K.M.S. holds stock in and is a consultant to Araxes Pharma LLC. K.M.S. holds stock in and is a consultant to Revolution Medicines, which is a developer of SHP2 inhibitors.

Data and materials availability: The RNA-seq data provided in the supplementary data files have been deposited to the Gene Expression Omnibus database under accession number GSE130616. All other data needed to evaluate the conclusions in the paper are present in the paper or the Supplementary Materials.

to the switch-II pocket (S-IIP) that is present only in the inactive guanosine diphosphate (GDP)-bound form of KRAS^{G12C}, sparing the wild-type protein. We used a genome-scale CRISPR interference (CRISPRi) functional genomics platform to systematically identify genetic interactions with a KRAS^{G12C} inhibitor in cellular models of KRAS^{G12C} mutant lung and pancreatic cancer. Our data revealed genes that were selectively essential in this oncogenic driver-limited cell state, meaning that their loss enhanced cellular susceptibility to direct KRAS^{G12C} inhibition. We termed such genes “collateral dependencies” (CDs) and identified two classes of combination therapies targeting these CDs that increased KRAS^{G12C} target engagement or blocked residual survival pathways in cells and in vivo. From our findings, we propose a framework for assessing genetic dependencies induced by oncogene inhibition.

INTRODUCTION

The concept that a cancerous phenotype can be driven by the activity of a single oncogene has motivated the search for targeted therapeutics directed against individual oncoproteins (1). Although this concept has been successfully implemented in numerous instances [as for the fusion protein BCR-ABL, the kinases HER2, EGFR, BRAF, KIT, and others] (2), it has not yet been possible in the case of the most frequently mutated human oncogene, the guanosine triphosphatase (GTPase) KRAS, due to its “undruggable” nature (3). To circumvent the inability to directly inhibit RAS proteins (KRAS, NRAS, and HRAS), other genetic dependencies associated with RAS mutations have been thoroughly investigated (4, 5). These approaches sought to indirectly target RAS-driven cancers through synthetic lethal (SL) genetic vulnerabilities that are selectively necessary for the maintenance of a RAS-mutated cell state (6, 7). Although these studies have nominated numerous promising targets (8–13), identifying broadly applicable, targetable SL vulnerabilities remains a challenge.

The paradigm of KRAS “undruggability” has evolved, as a new class of oncogene-specific direct KRAS^{G12C} inhibitor (14–17) has entered clinical trials (18, 19). In preclinical studies, an advanced-stage compound, ARS-1620, has exquisitely specific anticancer activity against KRAS^{G12C}-mutant tumors with no observed dose-limiting toxicity in mice (17). Despite this, and as is true for inhibitors of other driver oncogenes, it is likely that, upon direct pharmacological inhibition of KRAS^{G12C}, KRAS^{G12C}-dependent cancer cells will engage previously dispensable genes and pathways to maintain survival and proliferation. Therefore, inhibiting KRAS^{G12C} may render previously nonessential genetic dependencies newly vital to support cells suddenly deprived of mutant KRAS^{G12C} activity. Nonmutational bypass mechanisms of drug resistance are common in cancer (20); thus, it is imperative to define such mechanisms to overcome preexisting or de novo resistance to targeted therapeutics. We reasoned that bypass pathways capable of sustaining cancer cell survival in the face of acute deprivation of a driver oncogene’s activity are likely to be distinct from SL dependencies, which are contingent on the overactivation of KRAS signaling. We define this class of genetic interactions that support the driver-limited cancer cell state as collateral dependencies (CDs) and hypothesize that targeting CDs will promote response to KRAS^{G12C} inhibitors (Fig. 1A).

Here, we systematically identified and studied KRAS^{G12C} CDs by leveraging the allele-specific KRAS^{G12C} inhibitor, ARS-1620, to pharmacologically induce a driver-limited cell state. Under such conditions, genetic knockdown of individual genes uncovers underlying genetic dependencies that are selectively essential in the setting of KRAS^{G12C} inhibition. Using a genome-wide CRISPR interference (CRISPRi) functional genomics platform (21, 22), we identified diverse mechanisms by which CDs influence KRAS^{G12C}-driven growth upon oncogene inactivation. This approach identified specialized roles of known RAS signaling components and highlights CDs involved in transcriptional regulation and other cellular processes outside the core RAS pathway. In a large panel of KRAS^{G12C}-driven cancer cells, the vast majority of CDs identified in our experiments are not SL, thus demonstrating that CDs (driver oncogene–inhibited) are biologically distinct from SL dependencies (driver oncogene–active).

After validating our screen results genetically, we used pharmacology to further dissect the relationship between therapeutically targetable CDs and KRAS^{G12C}, revealing that chemical inhibition of both known and unexpected RAS pathway genes synergized with KRAS^{G12C} inhibition. We then investigated the mechanisms of these drug synergies inferred from our RAS pathway CD map using a new drug occupancy probe for direct KRAS^{G12C} inhibitor target engagement. These combination therapies either directly cooperated with switch-II pocket (S-IIP) inhibition to increase KRAS^{G12C} target engagement or independently blocked residual survival pathways. Both classes of combinations tested ultimately resulted in a deepened suppression of common signaling nodes, emphasizing the convergent nature of the oncogenic RAS signaling network.

Our study uncovered diverse mechanisms by which collateral pro-oncogenic signaling proteins sustain a mutant KRAS-dependent cancerous phenotype after acute chemical inhibition of KRAS^{G12C}. We demonstrated both in vitro and in vivo that combination therapies targeting KRAS^{G12C} and pro-survival CDs have enhanced anticancer activity. Our work reveals that optimal targeting of KRAS-driven cancers will require coinhibition of both the driver oncogene and upstream, downstream, and parallel CDs. This work also establishes generalizable strategies for cotargeting CDs to fully exploit the anticancer activity of driver oncogene inhibitors, a principle that we expect will apply to any direct inhibitor of an oncogenic driver.

RESULTS

Genome-scale CRISPRi screens nominate KRAS^{G12C} collateral dependent genes

We performed genome-scale screens using our previously described CRISPRi functional genomics platform (21, 22) in two cancer cell lines driven by KRAS^{G12C} mutation arising from distinct tissues to characterize CDs (Fig. 1A), whose knockdown could potentiate response to KRAS^{G12C} inhibition (Fig. 1B). Several features motivated the choice of the two cell lines used: (i) The H358 non–small cell lung cancer (NSCLC) and MIA PaCa-2 pancreatic ductal adenocarcinoma (PDAC) cell lines represent two cancers with high KRAS mutational prevalence; (ii) H358 is KRAS^{G12C}/KRAS^{WT}, whereas MIA PaCa-2 is KRAS^{G12C}/KRAS^{G12C}, representing two distinct genotypes associated with KRAS mutational status; (iii) both cell lines are highly sensitive to ARS-1620 [half-maximal

inhibitory dose (IC₅₀) within about two- to threefold] across both two-dimensional (2D) adherent and 3D spheroid cultures (17), suggesting that KRAS dependency is well represented in either condition; and (iv) selection in more than one KRAS^{G12C} line helps ensure likely generalizability to other cells that share this same driver mutation.

Pooled genome-scale genetic screens were performed by transducing H358 and MIA PaCa-2 cells stably expressing a CRISPRi construct (dCas9-KRAB) with a genome-scale CRISPRi library (21, 22). Transduced cell populations were grown in the presence or absence of ARS-1620 in duplicate. We measured quantitative differences in single-guide RNA (sgRNA) frequency for each sample by deep sequencing to determine how knockdown of a given gene contributes to cell growth and susceptibility to KRAS^{G12C} inhibition. Analysis of the H358 (fig. S1, A to D, and data files S1 and S2) and MIA PaCa-2 (fig. S2, A to D, and data files S3 and S4) screens showed high correlation between two biological replicates and confirmed depletion of known essential genes, validating our method as a high-confidence approach for identification of factors required for cellular survival in these models of KRAS-mutant NSCLC and PDAC. Growth phenotypes specifically associated with KRAS^{G12C} inhibition were quantitatively defined by the differences in sgRNA enrichment or depletion between ARS-1620- and dimethyl sulfoxide (DMSO)-treated cells ($\Delta\log_2$ fold change).

Analysis of ARS-1620 CD screen hits ($\Delta\log_2$ fold change < -0.5) revealed a number of core RAS pathway components as well as multiple processes not commonly associated with RAS signaling (Fig. 1C). Multiple genes were overlapping key regulators of response to ARS-1620 in these two diverse KRAS^{G12C}-mutant tumor models, but some KRAS^{G12C} CDs were also disease or model specific, such as *ZNF750*, a poorly characterized gene that is strongly sensitizing in the H358 screen (data file S2).

We then analyzed the relationship between the biology of overlapping CDs identified in our work to traditional SL CRISPR screen analysis of KRAS-mutant cancers. We determined average essentiality scores for our nominated CD genetic hits using CRISPR screening data in all KRAS-WT (wild-type) and KRAS-mutant NSCLC cancer cell lines (39 KRAS-WT and 19 KRAS-mutant) found in the publicly available datasets, PICKLES (pooled in vitro CRISPR knockout library essentiality screens) and DepMap (Cancer Dependency Map) (Fig. 1D) (23, 24). By taking the differences in essentiality scores between KRAS-mutant and KRAS-WT cell lines, we derived SL scores that reflect selective dependency in the presence of KRAS mutation. The only gene that was found to be both strongly SL (selectively essential in KRAS-mutant cells) and CD (selectively essential during mutant KRAS inhibition) in this analysis was KRAS itself, confirming, in this context, our hypothesis that the vast majority of CDs are not SLs.

CDs are selectively essential in the setting of KRAS^{G12C} inhibition

To validate the CD hits nominated by our CRISPRi screens, we transduced H358 and MIA PaCa-2 CRISPRi cells with individual sgRNAs and tracked relative populations of non-sgRNA-expressing and sgRNA-expressing cells over time (Fig. 2, A to C). We determined retest phenotypes from this mixed population assay using a metric, resistance index (RI), which reflects proportional differences in sgRNA-expressing populations across DMSO- and compound-treated conditions (Fig. 2, B and C) (25). Screen phenotypes ($\Delta\log_2$ fold change)

were correlated with retest phenotypes (RI) (Fig. 2, B and C), validating our genetic hits for their ability to selectively potentiate the effects of KRAS^{G12C} inhibition across multiple independent experimental conditions.

We then sought to characterize the mechanistic role of the transcription factor FOS-like antigen 1 (FOSL1), a CD required for survival in a driver-limited signaling state, by testing whether FOSL1 function affects key signaling pathways activated by KRAS. RAS serves as a central signaling hub, activating its two primary effector arms, the mitogen-activated protein kinase (MAPK) cascade and phosphoinositide 3-kinase (PI3K)/protein kinase B (AKT)/mammalian target of rapamycin (mTOR) pathway, as well as others to enable cell growth and proliferation. FOSL1 is a transcription factor activated by MAPK signaling that is reported to be among the most down-regulated mRNA transcripts by RNA sequencing (RNA-seq) upon treatment with ARS-1620 (17) and additionally has been implicated to play a role in the maintenance of mitotic machinery (26).

We were able to recapitulate ARS-1620's ability to down-regulate FOSL1 transcript by quantitative reverse transcription polymerase chain reaction (RT-qPCR) and found that sgRNAs identified in the screen targeting FOSL1 induced a similar extent of knockdown (Fig. 2D). Combining the effects of ARS-1620 inhibition of FOSL1 with CRISPRi genetic knockdown of FOSL1 further deepened suppression of FOSL1 mRNA expression and potently inhibited phosphorylated AKT (p-AKT) signaling (Fig. 2, D and E). p-AKT has been suggested to be a downstream node of RAS signaling that is recalcitrant to direct KRAS^{G12C} inhibition and important for cell survival and proliferation (27, 28). Our findings propose a mechanism that connects the MAPK and PI3K effector arms through FOSL1, a downstream output of the MAPK cascade. Genetic knockdown of FOSL1 notably led to no clear differences in the ability of KRAS^{G12C} inhibition to suppress signaling resulting in the phosphorylation of extracellular signal-regulated kinase (ERK) and ribosomal protein S6 (S6) (fig. S3), suggesting a highly specific requirement of FOSL1 to cross-activate AKT in both NSCLC and PDAC cell models.

A CD map reveals targetable vulnerabilities within critical signaling modules of the RAS pathway

To understand how our findings could be applied to design therapeutic strategies against KRAS^{G12C}-driven cancers, we constructed a CD map of the RAS pathway to visualize relationships between sensitizing and resistance genetic factors in both PDAC and NSCLC cell models and, for comparison, also included CD hits identified in both screens (Fig. 3A and fig. S4A). These data suggest two distinct mechanisms by which CDs can modulate cellular response to direct chemical inhibition of KRAS^{G12C}.

First, the KRAS^{G12C} protein cycles dynamically between active and inactive guanosine triphosphate (GTP)/guanosine diphosphate (GDP)-bound states (15, 16), and our data provide genetic support for the hypothesis that S-IIP inhibitors bind KRAS^{G12C}-GDP (14) as genes that can modulate this ratio of KRAS nucleotide occupancy, such as those encoding guanine nucleotide exchange factors (GEFs; as in *SOS1*) and their regulators (*FGFR1*, *EGFR*, *SHP2*, and *CRKL*), alter cellular sensitivity to ARS-1620. This first class of hits likely facilitates drug loading, thereby priming KRAS^{G12C} mutant cells with a permissive

amount of KRAS^{G12C}-GDP to promote efficient compound target engagement and anticancer activity. Even among highly overlapping classes of genes, such as receptor tyrosine kinases (RTKs) (29), specific genetic knockdowns pinpointed critical functional nodes that were not readily apparent by assessment of mRNA expression alone (Fig. 3B and fig. S4B) (30).

A second category of hit genes critically important to diverse cell growth and survival pathways, including cell cycle control (such as *CCND1* and *CDK4*), multiple cell adhesion proteins (such as *ITGA7* and *ITGAV*), regulators of transcription (such as *FOSL1*), and the PI3K/AKT/mTOR pathway, modulated sensitivity to ARS-1620, suggesting that cell death induced by direct inhibition of KRAS^{G12C} is influenced by various pathways commonly dysregulated in KRAS-mutant cancers (Fig. 3A and fig. S4A) (31). This second class of hits is predicted to not change ARS-1620 target engagement and would thus be mechanistically distinct from those that alter KRAS^{G12C}-GDP abundance. We also observed that substrates of protein kinase screen hits were differentially phosphorylated after ARS-1620 treatment, consistent with dynamic regulation of KRAS^{G12C} activity (fig. S5, A and B, and data file S5). We note that, for other overlapping, sensitizing CD hits (such as *ELP3*, *ELP4*, *KIF18A*, *PKN2*, *VBPI*, and *VPS29*), the direct connection to KRAS remains to be uncovered and will motivate future investigations.

Our results confirm the initial CD hypothesis that previously dispensable or weak genetic dependencies can become potentiated when reframed in the context of an oncogenic driver-limited state. Numerous compounds directed against targets and pathways identified by our screens have failed to demonstrate clinical efficacy as monotherapies in KRAS-mutant cancers (32). Dual inhibition of KRAS^{G12C} and various cotargets could repurpose these agents by applying them to therapeutic scenarios with heightened non-driver genetic dependencies.

Two classes of combination therapies targeting CDs with KRAS^{G12C} promote distinct mechanisms of synergy

These data suggest that, despite differences in tissue of origin and genetic background, functional interactions with mutant KRAS signaling dependency can be governed by common CDs that are druggable using clinically approved and advanced preclinical compounds. To test the mechanistic hypothesis that repression of select CDs promotes increased target engagement by ARS-1620, we developed ARS-1323-alkyne, a chemical probe that enables measurement of live-cell KRAS^{G12C} covalent inhibition kinetics (Fig. 4A). After treatment of cells with ARS-1323-alkyne, covalent labeling was assessed using an electrophoretic mobility shift assay where larger protein-small molecule adducts migrate more slowly following click reaction to tetramethylrhodamine azide (TAMRA-N₃) (Fig. 4B) (33). Relative target engagement was quantified by the densitometry of upper (KRAS + inhibitor) and lower (KRAS) bands.

We sought to measure the influence of cotargeting CD vulnerabilities upstream [with an EGFR inhibitor (EGFRi), a fibroblast growth factor receptor inhibitor (FGFRi), an AXL inhibitor (AXLi), and a protein tyrosine phosphatase, non-receptor type 11 inhibitor (SHP2i)], downstream [with a cyclin-dependent kinase 4/6 inhibitor (CDK4/6i)], and

parallel [with a PI3K inhibitor (PI3Ki)] to KRAS^{G12C} on inhibitor target engagement in NSCLC and PDAC models. The kinetics of KRAS^{G12C} inhibition in the H358 NSCLC model with ARS-1323-alkyne demonstrated two general classes of combinations (Fig. 4, C and D). We observed that KRAS^{G12C} probe target engagement was perturbed by cotreatment with compounds that inhibit GTP loading to KRAS^{G12C} (such as SHP2i) by effectively preventing recruitment and activation of the RAS GEF son of sevenless (SOS). Conversely, coinhibition of cognate pro-growth and pro-survival pathways was shown to operate outside the direct context of nucleotide cycling (such as with CDK4/6i). These results were generalized to the MIA PaCa-2 PDAC model, with pharmacological interactions reflecting differences in observed genetic dependencies; for example, EGFR and FGFR1 were found to be cell-specific CDs, whereas SHP2 was overlapping (Fig. 4, E and F). Inhibition of the RTK AXL, which has been implicated in promoting mitochondrial activity in KRAS-mutant PDAC models (34), does not appear to strongly influence KRAS^{G12C} nucleotide state, consistent with a model in which different RTKs play specialized roles to support a mutant KRAS-driven phenotype.

Together, our experiments nominate two classes of combination therapies that either enhance KRAS^{G12C} target engagement (namely, EGFR, FGFR, or SHP2 inhibitors) or independently suppress persistent survival pathways (namely, AXL, PI3K, or CDK4/6 inhibitors).

Mechanistically diverse CDs with KRAS^{G12C} converge upon downstream signaling outputs

We explored the link between KRAS^{G12C} target engagement and inhibition of various downstream signaling outputs by treating cells with ARS-1323-alkyne at an intermediate time point with different second chemical agents. Treating each cell line with its RTK dependency's cognate growth factor (EGF for the NSCLC line H358 and FGF2 for the PDAC line MIA PaCa-2) potentially obstructed the effects of KRAS^{G12C} inhibition at both the target engagement and signaling levels (Fig. 5A). Overall, combinations that cotarget upstream genes (RTKs and SHP2) potentiated suppression of p-ERK, whereas those that cotarget parallel and downstream factors (PI3K and CDK4/6) displayed modest to no differences in p-ERK activation compared to monotreatment. Cotargeting PI3K also distinctly inhibited p-AKT signaling. Despite these differences, however, all combinations tested resulted in notably deeper suppression of p-S6, which has been shown to correlate well with inhibition of cell viability (28, 35).

Studies have demonstrated that RAS-driven cancer cells are more dependent on RAS signaling in 3D than in 2D culture models (15, 17, 36, 37). To evaluate the context specificity of our results, we assessed several drug combinations in 2D and 3D assays. Consistent with their ability to promote p-S6 inhibition, combinations cotargeting CDs showed enhanced anticancer activity in both 3D (Fig. 5B) and 2D (Fig. 5C) assays in H358 and MIA PaCa-2, as well as in a third KRAS^{G12C}-driven NSCLC cancer cell line, H23. In the 3D assay, we found that multiple drug combinations formally have synergistic antitumorigenic activity (38).

These pharmacological experiments validated cell type-specific synergies exemplified by specialized RTKs that promote KRAS^{G12C} activation and other pathways. Conversely, coinhibition of SHP2, a broadly required RTK adaptor, represented a general synergy as did

coinhibition of PI3K or CDK4/6. Our data suggest that CDs nominated by our CRISPRi screens reveal diverse targetable genetic dependencies in NSCLC and PDAC models that result in the enhanced suppression of critical downstream signaling outputs required for cell viability.

Coinhibition of CDK4/6 potentiates the global effects of KRAS^{G12C} inhibition

CDK4 and its close homolog CDK6 cooperate with D-type cyclins to promote G1-S cell cycle progression through direct phosphorylation of retinoblastoma (RB) tumor suppressor family members, releasing a transcriptional program mediated by the transcription factor E2F to initiate S-phase entry in the cell cycle (39). CDK4 has also previously been suggested to be an SL partner with mutant KRAS (40), although inhibition of CDK4/6 proved to be ineffective as a monotherapy in KRAS-mutant NSCLC in a phase 3 trial (41). Neither CDK4 nor cyclin D1 (CCND1) displayed strong SL relationships with mutant KRAS in our analysis of the PICKLES database and DepMap (Fig. 1D), but both genes appeared as strong KRAS^{G12C} CDs in our CRISPRi screens in both the NSCLC and PDAC models (Figs. 1 and 3 and fig. S4). This may suggest that the essentiality of CDK4 is amplified in the setting of mutant KRAS inhibition, reframing the genetic interaction as a true CD relationship.

Intrigued by the ability of palbociclib (CDK4/6i) to decrease p-S6 when combined with a KRAS^{G12C} inhibitor, we compared by RNA-seq the transcriptome profiles of H358 cells treated with DMSO, CDK4/6i, ARS-1620, and the combination. Treatment with the combination of CDK4/6i and ARS-1620 resulted in an expression profile that reflected potent inhibition of cell proliferation (Fig. 6, A and B). The concentration of ARS-1620 used (1 μ M) has been demonstrated to affect $\geq 95\%$ target engagement in H358 cells at the assayed time point (24 hours) (17). Unbiased clustering of top significantly altered transcripts by the combination revealed major changes in four primary gene ontologies (Fig. 6A) (42). Inhibition of KRAS^{G12C} alone appeared to modestly suppress cell division genes (such as *CCNA2*, *CCNB1/2*, and *CDK1*), whereas CDK4/6i alone or in combination induced their marked down-regulation (Fig. 6, B and C). Conversely, CDK4/6i alone resulted in no statistically significant differences in MAPK inhibition-associated genes (such as *CCND1* and *DUSP4/5/6*), whereas the combination displayed significantly decreased expression even when compared to ARS-1620 monotherapy. Overall, both additive and synergistic (in the case of inhibition of MAPK activity) effects were observed where the transcriptional changes induced by KRAS^{G12C} inhibition were complemented and strengthened by cotreatment with CDK4/6i (Fig. 6, C and D).

To understand the signaling mechanisms from which these transcriptional changes might be derived, we probed two primary signaling outputs, p-S6 and p-RB, that reflect the activity of KRAS^{G12C} and CDK4/6, respectively, in NSCLC and PDAC models (Fig. 6E). We observed that, consistent with RNA-seq experiments, CDK4/6i alone or in combination more strongly induced markers of G1 arrest (decreases in p-RB) than ARS-1620 monotherapy (Fig. 6E). Furthermore, addition of CDK4/6i shifted the dose-response relationship between KRAS^{G12C} inhibition and p-S6. S6 integrates inputs from both the MAPK and PI3K/AKT/mTOR effector arms of the RAS pathway; thus, it was unexpected that inhibition of CDK4/6

would alter these phosphorylation dynamics. CDK4/6i's ability to suppress RAS pathway signaling appears specific to p-S6, as only subtle changes were observed in p-AKT and p-ERK (fig. S6, A and B). Our data indicate that KRAS^{G12C} inhibition is insufficient to fully suppress G1-S progression, that CDK4/6 inhibition is unable to halt signaling through KRAS^{G12C}, and that the combination maintains both advantages while bolstering the effects of driver oncogene inhibition.

Cotargeting CDs promotes response to KRAS^{G12C} inhibition in vivo

To validate ARS-1620 combination therapies in vivo, we designed two preclinical trials to model combination therapies cotargeting CDs and KRAS^{G12C}. At high doses of ARS-1620 that elicit a robust antitumor response (50 to 200 mg/kg), it has been shown that KRAS^{G12C} target engagement is incomplete (17). Therefore, we rationalized that, at this dose range of ARS-1620, it is likely that in vivo tumor cell survival is fostered by CDs that limit target engagement as well as CDs that promote alternate survival pathways. We performed experiments to test two combination therapies that promote ARS-1620 target engagement (ARS-1620 and EGFRi) in H358 xenograft tumors (Fig. 7A) or inhibit a residual survival pathway (ARS-1620 and CDK4/6i) in MIA PaCa-2 xenograft tumors (Fig. 7B). In both experiments, the combination proved more effective than either monotherapy, confirming that both mechanisms of combination therapies targeting KRAS-mutant cancers can augment ARS-1620 activity in vivo. In support of our mechanistic understanding of the ARS-1620/EGFRi combination therapy, we found that the ARS-1620/EGFRi combination decreased the activity of key downstream KRAS signaling outputs (p-AKT, p-ERK, and p-S6) (fig. S7), suggesting that this combination acts via deepened suppression of KRAS signaling, consistent with enhanced target engagement of KRAS^{G12C}. These experiments nominate combination therapies that combine ARS-1620, an oncogene-specific KRAS^{G12C} inhibitor, with a second targeted agent such as EGFRi or CDK4/6i to increase anticancer activity while minimizing synergistic on-target toxicity to the patient.

DISCUSSION

Three principles emerge from our analysis of genetic dependencies in a KRAS driver-limited state. First, we found that KRAS CDs and SLs are largely nonoverlapping genetic dependencies. Our screens identified KRAS CDs, which support a cancerous phenotype in the setting of driver oncogene inhibition. Our data highlight the concept that CDs are complementary to traditional SL interactions for understanding driver oncogene biology and anticipate the importance of using both overactivated and hypomorphic model systems to study genetic dependencies related to any driver oncogene.

Our experiments revealed CDs upstream of KRAS^{G12C} in NSCLC and PDAC cell models and emphasizes a growing perspective that mutant KRAS is dynamically regulated and responsive to upstream inputs in cancer cells (43–47). Beyond the requirement of KRAS^{G12C} for SOS-catalyzed nucleotide exchange to sufficiently maintain its GTP state, we suggest that the RTKs EGFR, FGFR1, and AXL play specialized roles in mutant KRAS signaling and activation. We reveal that the relevant receptors in these signaling networks are

cell type specific and highlight the modularity of RTKs in the recruitment of a shared set of adaptor proteins (such as SHP2) to transduce signal to SOS and RAS proteins.

We also identified CDs downstream and parallel to KRAS^{G12C} that were incompletely suppressed by driver oncogene inhibition. Our findings suggest that independent inputs from RTKs and/or cell adhesion/cohesion can circumvent KRAS^{G12C} to maintain PI3K activity, limiting the ability of direct KRAS^{G12C} inhibitors to fully disrupt all RAS effector arms. We also suggest that mutant KRAS is, on its own, not fully responsible for promoting cell cycle progression and that CDK4 can sustain G1-S transition even in the setting of RAS pathway inhibition. This may explain, in part, the finding that genetic alterations in *CDK4* and/or *CCND1* in BRAF-mutant melanoma and EGFR-mutant lung cancer promote resistance to their respective driver inhibitors (48, 49). We anticipate that similar mechanisms may also promote resistance to direct KRAS inhibitors and propose coinhibition of CDK4/6 as a strategy to maximize therapeutic efficacy. In addition, we nominate CDs not commonly associated with RAS function related to transcriptional control and other diverse processes that merit further exploration. We anticipate that our results will generalize to other KRAS-mutant cancers and propose the possibility of cotargeting multiple CDs to address mutant KRAS alleles yet to succumb to direct allele-specific pharmacology.

Second, our genetic analysis suggests a specific mechanistic hypothesis for CDs suspected to regulate the ratio of KRAS GTP/GDP. The engagement of a small molecule with its target can report on the conformation, oligomerization state, and/or activity of a specific protein in its native environment. Classically, type I kinase inhibitors bind to target protein kinases in the active state, whereas type II kinase inhibitors bind kinases in an inactive state (50). Resistance to type II kinase inhibitors can therefore be achieved through mutations or signaling mechanisms that promote kinase activity (51). In analogy to this, our work expands this intellectual framework to GTPases, such as KRAS, by mechanistically revealing how upstream signaling pathways that decrease levels of KRAS GDP promote resistance to ARS-1620. We use S-IIP inhibitors (ARS-1620 and ARS-1323-alkyne) as conformationally specific chemical reporters of KRAS^{G12C} nucleotide state in living cells. As the development of direct KRAS inhibitors extends toward GTP-state binders, such agents would not benefit from target engagement enhancement through GDP-state priming, although they would likely continue to synergize with combinations that coinhibit other CDs that sustain residual survival.

We anticipate that the two mechanisms of synergy we describe (target engagement enhancing or independent inhibition of residual growth signals) are generalizable to other chemical-genetic or drug combination interactions. We propose systematic identification of such interactions using conformationally biased covalent probes coupled to functional genomics screens, dissecting complex target regulation and enabling the construction of mechanistically informed combination therapies.

Third, we reveal that single-target inhibition of even one of the most well-validated oncogenic drivers can be limited by CDs that help sustain an oncogenic phenotype in the driver-limited state. We addressed these limitations by presenting two distinct classes of in vivo validated ARS-1620 combinations, which require further evaluation in genetically

engineered mouse models (52). We anticipate that allele-specific inhibitors like ARS-1620, which spare the WT protein, will be well tolerated in patients and highly amenable to combination with second inhibitors to enable synergistic anticancer activity without synergistic toxicity to otherwise normal cells and tissues.

The concept that a cancerous phenotype can be driven by the activity of a single oncogene is being revised given that, beyond BCR-ABL inhibitors in chronic myelogenous leukemia, targeted therapies have fallen short on their promise of promoting durable responses and cures for patients. We nominate CDs to be the underlying cellular processes that are engaged upon driver oncogene inhibition and limit the efficacy of targeted therapeutics. We anticipate the logic of CDs to be generalizable to any driver oncogene through genetic or chemical perturbation, providing an opportunity for cotarget identification in next-generation combination therapies (53).

MATERIALS AND METHODS

Cell culture and reagents

All cell lines used in this study (H358, MIA PaCa-2, and H23) were obtained from the American Type Culture Collection and authenticated by the University of California (UC) Berkeley DNA Sequencing Facility using short tandem repeat DNA profiling. Cells were maintained in Dulbecco's modified Eagle's medium (DMEM) supplemented with 10% (v/v) fetal bovine serum, penicillin (100 U/ml), and streptomycin (100 µg/ml). All cells were grown at 37°C in 5% CO₂. All cells were tested for Mycoplasma contamination using the MycoAlert PLUS Mycoplasma Detection Kit (Lonza) before initiation of experiments. ARS-1620 was obtained by custom synthesis from Pharmaron. Erlotinib and palbociclib were obtained from LC Laboratories, AZD4547 and buparlisib were obtained from MedChem Express, and SHP099 and bemcentinib were obtained from Selleckchem. ARS-1323-alkyne was synthesized as described below. Recombinant human EGF and FGF2 (FGF-basic) were obtained from Thermo Fisher Scientific. TAMRA-N₃ and tris(benzyltriazolylmethyl)amine (TBTA) were obtained from Click Chemistry Tools. Tris(2-carboxyethyl)phosphine (TCEP) and CuSO₄ were obtained from Sigma-Aldrich.

DNA transfections and lentivirus production

For lentivirus production, HEK293T cells were transfected with standard packaging vectors using the TransIT-LT1 Transfection Reagent (Mirus Bio). Viral supernatant was collected 2 to 3 days after transfection, filtered through 0.44-µm polyvinylidene difluoride filters, and frozen before transduction.

Generation of CRISPRi cell lines

H358 and MIA PaCa-2 cell lines stably expressing dCas9-KRAB were generated by transducing WT cells with a lentiviral vector expressing dCas9-BFP-KRAB from an EF1α promoter with an upstream ubiquitous chromatin opening element (UCOE; UCOE-EF1α-BFP-KRAB) and selected for blue fluorescent protein (BFP)—positive cells through two rounds of fluorescence-activated cell sorting (FACS) with a BD FACSAria II.

Genome-scale CRISPRi screening

Genome-scale CRISPRi screens were conducted similarly to previously described screens (21, 22). The five-sgRNA/gene human CRISPRi v2 (hCRISPRi-v2) library (22) was transduced into H358 or MIA PaCa-2 CRISPRi cells at a multiplicity of infection (MOI) of <1 (percentage of transduced cells 2 days after transduction = 20 to 40%). Cells were selected with puromycin (3 $\mu\text{g}/\text{ml}$) to achieve 80 to 95% transduced cells, at which point T0 samples were harvested with a minimum 500 \times library coverage (100×10^6 to 150×10^6 cells), and the remaining cells were split into two biological replicates of two conditions for DMSO- and ARS-1620-treated growth. Cells were grown in 150-mm adherent dishes, maintaining an average minimum 500 \times library coverage, trypsinized and reseeded every 3 to 5 days over the course of the screen, and dosed with respective treatments after each trypsinization and reseeded. For ARS-1620 treatment, ARS-1620 was added to H358 CRISPRi cells at 3.3 μM and to MIA PaCa-2 CRISPRi cells at increasing concentrations from 348 nM to 10 μM as the screen proceeded. After 12 to 16 days of growth and selection, cells were harvested with a minimum 500 \times library coverage (100×10^6 to 150×10^6 cells). Genomic DNA was isolated from frozen cell pellets, and the sgRNA-encoding region was enriched, amplified, and processed for sequencing on the Illumina HiSeq 4000 as described previously (21).

Screen processing

Sequencing data from the Illumina HiSeq 4000 were aligned to the five-sgRNA/gene hCRISPRi-v2 library, counted, and quantified using the Python-based ScreenProcessing pipeline [<https://github.com/mhorlbeck/ScreenProcessing> (22)]. sgRNA phenotypes, gene phenotypes, negative control gene phenotypes, and Mann-Whitney P values were determined as described previously (21, 22). ARS-1620 sensitivity sgRNA phenotypes ($\Delta\log_2$ fold change) were calculated by subtracting the equivalent median value for all nontargeting (NT) sgRNAs from the \log_2 fold change in enrichment of an sgRNA in the ARS-1620- and DMSO-treated samples. DMSO and ARS-1620 sgRNA growth phenotypes were similarly calculated from respective \log_2 fold changes in enrichment of an sgRNA from T0 samples. Gene phenotypes were derived by collapsing phenotypes from sgRNAs targeting the same gene using the average of the three top scoring sgRNAs (by absolute value) and assigning a P value using the Mann-Whitney test of all sgRNAs targeting the same gene compared to the NT sgRNAs. For genes with multiple annotated transcription start sites (TSSs) targeted by the sgRNA library, phenotypes and P values were calculated independently for each TSS, and the TSS with the lowest Mann-Whitney P value was used to represent the gene. Read counts and phenotypes for individual sgRNAs are provided in data files S1 (H358) and S3 (MIA PaCa-2). Gene-level phenotypes are provided in data files S2 (H358) and S4 (MIA PaCa-2). Hits were defined as genes with $|\Delta\log_2$ fold change| > 0.5. Gene ontology analysis was performed using DAVID Bioinformatic Resources using the GOTERM_BP_DIRECT database (42). Additional analysis and plotting were performed in Prism 7 and 8 (GraphPad Software).

Essentiality score and SL score determination

Essentiality and mutational data were drawn from the PICKLES database (23) and DepMap/CCLE (24, 30), respectively (2018 Q3 release). The PICKLES database contains essentiality scores for all genes and cell lines in DepMap that have been converted to Bayes factors from log fold changes (54). NSCLC cell lines from the PICKLES database and DepMap were placed in one of two bins: KRAS-WT (39 cell lines) and KRAS-mutant (19 cell lines). A given gene's essentiality score (quantile normalized Bayes factor) was averaged across all cell lines in a given bin, resulting in an average essentiality score for KRAS-WT and KRAS-mutant NSCLC models. Each gene's SL score was then determined by subtracting its KRAS-WT average essentiality score from its KRAS-mutant average essentiality score.

Individual evaluation of sgRNA phenotypes

sgRNA protospacers targeting *CCND1*, *CDK4*, *CRKL*, *ELP3*, *ELP4*, *FOSL1*, *KAT6A*, *KIF18A*, *MED24*, *TLN1*, *TM2D1*, *TM2D2*, *TM2D3*, *UNC50*, and a negative control NT sequence were individually cloned into BstXI/BlpI-digested pCRISPRi-v2 [marked with a puromycin resistance cassette and green fluorescent protein (GFP) or BFP, Addgene #84832] (22) by ligating annealed complementary synthetic oligonucleotide pairs (Integrated DNA Technologies) with flanking BstXI and BlpI restriction sites. Protospacer sequences used are listed in table S1. The sgRNA expression vectors were individually packaged into lentivirus as described above. Internally controlled growth assays to evaluate relative sgRNA susceptibility to ARS-1620 were performed by transducing H358 and/or MIA PaCa-2 cells with sgRNA expression vectors at an MOI of <1 (20 to 40% transduction rate). Five days after transduction, cells were treated with DMSO or ARS-1620 (300 nM or 1 μ M for H358 and 300 nM or 3.3 μ M for MIA PaCa-2) for 12 days before the percentage of sgRNA-expressing cells was determined as the percentage of GFP- or BFP-positive cells by flow cytometry on an LSR II (BD Biosciences) or an Attune NxT (Thermo Fisher Scientific). RI was calculated as a measurement of the relative level of sensitization (RI < 1) or resistance (RI > 1) to ARS-1620, where $RI = (F2 - F1 \times F2) / (F1 - F1 \times F2)$, with F1 being the endpoint GFP- or BFP-positive percentage of the DMSO-treated population and F2 being the endpoint GFP- or BFP-positive percentage of the ARS-1620-treated population (25).

Quantitative PCR

CRISPRi cells (500,000 cells per well) stably expressing a negative control sgRNA or sgRNAs targeting *FOSL1* (table S1) were seeded into six-well ultra-low attachment plates (Corning Costar #3471) and allowed to incubate at 37°C overnight. Cells were treated with DMSO or ARS-1620 (1 μ M) and then incubated at 37°C for 24 hours. Cells were lysed, and total RNA was immediately extracted with the RNeasy Mini Kit (Qiagen) according to the manufacturer's recommendations. RT-qPCR was performed using the SYBR Select Master Mix (Thermo Fisher Scientific) according to the manufacturer's recommendations on the QuantStudio 7 Flex Real-Time PCR System (Thermo Fisher Scientific). Fold changes were calculated using $\Delta\Delta C_t$ analysis, normalizing *FOSL1* (*FOSL1* forward primer, GGCCTCTGACCTACCCTCA; *FOSL1* reverse primer, CTCCTCCGGGCTGATCT) in

each sample to actin (ACTIN forward primer, GCTACGAGCTGCCTGACG; ACTIN reverse primer, GGCTGGAAGAGTGCCTCA).

Global phosphoproteomics

Cells were expanded in conventional 2D culture conditions, adapted to 3D culture in ultra-low adherence plates (Corning) over 72 hours, and treated with DMSO or 3.3 μ M ARS-1620 for 24 hours. Cells were then collected, lysed, and subjected to tryptic digest. Phosphoenrichment was then performed with immobilized metal affinity chromatography using established protocols (55). Samples were then lyophilized, desalted, and acquired using an Orbitrap Fusion Lumos Tribrid (Thermo Fisher Scientific). All mass spectrometry was performed at the Thermo Fisher Scientific Proteomics Facility for Disease Target Discovery at UC San Francisco (UCSF) and the J. David Gladstone Institutes. Peptide identification and label-free quantification were then performed using MaxQuant (56), and statistical comparison was performed using MSstats (57). Kinase substrate identification was performed using two established databases: PhosphoNetworks (58) and RegPhos 2.0 (59).

ARS-1323-alkyne kinetic labeling assay

Cells (500,000 to 1,000,000 cells per well) were seeded into six-well ultra-low attachment plates (Corning Costar #3471) and allowed to incubate at 37°C overnight. Cells were treated with the indicated concentrations of compound combinations and then incubated at 37°C for the indicated times. In preparation for sodium dodecyl sulfate-polyacrylamide gel electrophoresis (SDS-PAGE) and immunoblotting, cells were pelleted at 4°C at 500g and washed twice with ice-cold phosphate-buffered saline (PBS). Lysis was conducted as described below, and copper-catalyzed click chemistry was performed by addition of the following to each lysate at the following final concentrations: 1% SDS (20% SDS in water stock), 50 μ M TAMRA-N₃ (5 mM in DMSO stock), 1 mM TCEP (50 mM in water stock), 100 μ M TBTA (2 mM in 1:4 DMSO/t-butyl alcohol stock), and 1 mM CuSO₄ (50 mM in water stock). After 1 hour at room temperature, the reaction was quenched with 6 \times Laemmli sample buffer before SDS-PAGE.

SDS-PAGE and immunoblotting

Lysis buffer [100 mM Hepes (pH 7.5), 150 mM NaCl, and 0.1% NP-40] supplemented with protease inhibitors (cOmplete Protease Inhibitor Cocktail Tablets, Roche) and phosphatase inhibitors (PhosSTOP, Roche) was used for cell lysis, and protein concentration was determined by bicinchoninic acid assay (Pierce BCA Protein Assay Kit, Thermo Fisher Scientific). Proteins were separated by SDS-PAGE and transferred to nitrocellulose membranes (Bio-Rad) and blocked according to standard protocols. Membranes were immunoblotted with antibodies against RAS (ab108602) from Abcam, α -tubulin (3873), p-AKT^{S473} (4060), AKT (4691), p-ERK^{T202/Y204} (9101), ERK (4695), HSP90 (4877), p-RB^{S807/811} (8516), RB (9313), p-S6^{S235/236} (4858), and S6 (2217) from Cell Signaling Technology diluted (1:1000) in 5% bovine serum albumin in TBST blocking buffer supplemented with 0.02% NaN₃. After primary antibody incubation, membranes were probed with IRDye secondary antibodies (LI-COR Biosciences) according to the manufacturer's recommendations and scanned on an Odyssey Imaging System (LI-COR Biosciences). Phosphoprotein blots (p-AKT^{S473}, p-ERK^{T202/Y204}, and p-S6^{S235/236}) were

stripped (Restore PLUS Western Blot Stripping Buffer, Thermo Fisher Scientific) according to the manufacturer's recommendations and immunoblotted for total protein (AKT, ERK, and S6). RB and p-RB^{S807/811} blotting was performed as above in the reverse order.

Clonogenic assay

Cells (10,000 cells per well) were seeded into six-well plates and allowed to adhere overnight. Cells were then cultured in the presence or absence of compounds as indicated for 10 to 14 days. After removal of media, cells were washed twice with PBS and then treated with fixing/staining solution (0.05% crystal violet, 1% formaldehyde, 1× PBS, and 1% methanol) for 20 min before thorough washing with water. Plates were then imaged using a digital scanner.

Cell viability assay and quantitative analysis of drug synergy

Cells were seeded into 96-well ultra-low attachment plates (Corning Costar #3474) and were allowed to incubate at 37°C overnight. Cells were treated with ARS-1620 and the indicated compounds as monotherapy or in combination (1:1 concentration ratio) in a nine-point threefold dilution series from 1.5 nM to 10 μM (100 μl final volume per well). Cell viability was assessed 5 days later by a CellTiter-Glo (CTG) luminescence-based assay (Promega). Diluted CTG reagent (100 μl) (1:4 CTG reagent:PBS) was added to cells and the 96-well plates were placed on a plate shaker for 20 min to ensure complete cell lysis before assessment of luminescence signal. Drug synergism was analyzed using CompuSyn 1.0 (a value of 0.01 was substituted for negative viability measurements). CIs were determined at 370 nM single-agent doses generated by CompuSyn to quantify synergistic effects, where CI < 0.75 reflects synergism, CI = 0.75 to 1.25 reflects additivity, and CI > 1.25 reflects antagonism (38).

RNA sequencing

Cells (500,000 cells per well) were seeded into six-well ultra-low attachment plates (Corning Costar #3471) and allowed to incubate at 37°C overnight. Cells were treated with DMSO, palbociclib (1 μM, CDK4/6i), ARS-1620 (1 μM), or the combination in duplicate and then incubated at 37°C for 24 hours. Cells were lysed, and total RNA was immediately extracted with the RNeasy Mini Kit (Qiagen) according to the manufacturer's recommendations. RNA-seq libraries were prepared with the QuantSeq 3' mRNA-Seq Library Prep Kit FWD for Illumina (Lexogen) and assessed on a BioAnalyzer 2100 (Agilent) for quantification and quality control. RNA-seq libraries were sequenced on an Illumina HiSeq 4000 using single-end, 50-base pair (bp) sequencing. The leading 12 bp of all sequencing reads was trimmed with Trimmomatic (Galaxy version 0.36.5) and then aligned to the hg19 reference genome with STAR (Galaxy version 2.6.0b-1). Mapped reads per gene were summarized using featureCounts (Galaxy version 1.6.2). Data normalization and differential expression analysis were conducted with the R package DESeq2 (version 1.20.0) (60). Read counts were normalized using the estimateSizeFactors() and rlog() functions. Heatmap plots were generated using the aheatmap() function from the R package NMF (version 0.17.6).

Animal studies

Six- to seven-week-old female nude mice (Foxn1nu, stock no. 002010) were purchased from the Jackson Laboratory and housed with ad libitum food and water on a 12-hour light cycle at the UCSF Preclinical Therapeutics Core vivarium. All animal studies were performed in full accordance with UCSF Institutional Animal Care and Use Committee.

H358 xenografts were established by subcutaneous injection into the right flanks of mice with H358 cells (5×10^6 cells in 100 μ l of serum-free medium mixed 1:1 with Matrigel). Tumor xenografts were allowed to establish until they reached about 700 to 900 mm³ in donor mice and then reimplanted into receiver mice to achieve higher engraftment rate. Briefly, established H358 tumor xenografts from donor mice were resected, cut into even-size fragments (15 mm \times 15 mm), embedded in Matrigel, and reimplanted via subcutaneous implantation into receiver mice (61). H358 tumor-bearing mice were randomized into control and treatment groups when tumors reached a size range of 100 to 120 mm³, and single or dual dosing of ARS-1620 (100 mg/kg in Labrasol) and erlotinib [80 to 100 mg/kg in 0.5% (hydroxypropyl)methyl cellulose, 0.2% Tween 80 (HPMT)] or vehicle control (Labrasol) was administered daily by oral gavage. Tumor volume and body weight were assessed biweekly for the duration of the study. Tumor volume was assessed by caliper 2D measurement, and volume was calculated using the following formula to approximate the volume of an ellipsoid: $0.52 \times (\text{width})^2 \times (\text{length})$. When tumor volumes of vehicle-treated mice reached a size of 400 mm³, ARS-1620, erlotinib, and dual treatments were stopped and tumors were harvested for subsequent analysis. Vehicle-treated mice were reenrolled in a short pharmacodynamic study (four groups, two mice per group) and treated for 3 days with single or dual dosing of ARS-1620 (100 mg/kg in Labrasol) and erlotinib (100 mg/kg in HPMT) or vehicle (Labrasol). Tumors were harvested 6 hours after the last dose and snap-frozen for protein extraction and immunoblotting.

MIA PaCa-2 xenografts were established by subcutaneous injection into the right flanks of mice with MIA PaCa-2 cancer cells (5×10^6 cells in 100 μ l of serum-free medium mixed 1:1 with Matrigel). MIA PaCa-2 tumor-bearing mice were randomized into control and treatment groups when tumors reached a size range of 180 to 200 mm³, and single or dual dosing of ARS-1620 (100 mg/kg in Labrasol) and palbociclib [100 mg/kg in sodium lactate buffer (50 mM, pH 4.0)] or vehicle control (Labrasol) was administered daily by oral gavage. Tumor volume and body weight were assessed biweekly for the duration of the study. Tumor volume was assessed by caliper 2D measurement. When vehicle-treated mice reached the size limit of 2000 mm³, all treatments were stopped and tumors were harvested for subsequent analysis.

Quantification and statistical analysis

Immunoblots were processed using ImageStudioLite 5.2.5 (LI-COR). Densitometry quantification was performed by fixing the relative shape, size, and distance between band pairs of each region assessed within each experiment. Background was set to the median value around all sides of the quantified region with a border width of 1. Negative densitometry values were assessed as 0. Relative KRAS^{G12C} labeling percentage was calculated as $100 \times (\text{top band})/(\text{top band} + \text{bottom band})$ densitometry quantifications.

Sequencing data from CRISPRi screens were processed using the Python-based ScreenProcessing pipeline [<https://github.com/mhorlbeck/ScreenProcessing> (22)]. Details of methods to calculate phenotypes and *P* values have been described previously (21, 22). Relative KRAS^{G12C} labeling percentage data were fit to pseudo–first-order association kinetics, and additional statistical analysis was conducted using Prism 7 and 8 (GraphPad Software).

Chemical synthesis

Detailed descriptions of compound synthesis and characterization can be found in the Supplementary Materials (text S1).

Supplementary Material

Refer to Web version on PubMed Central for supplementary material.

Acknowledgments:

We thank M. Horlbeck, A. Balmain, D. Jimenez-Morales, N. Krogan, D. Ruggero, J. Taunton, J. Weissman, the UCSF/Gladstone Institute Thermo Fisher Scientific Proteomics Facility, and the UCSF Preclinical Therapeutics Core for assistance and discussion.

Funding: This work was supported by NIH grant F30CA239476 (to K.L.); the Howard Hughes Medical Institute, NIH grant R01CA190408, the Samuel Waxman Cancer Research Foundation, and Stand Up To Cancer (SU2C)–American Cancer Society Lung Cancer Dream Team Translational Research grant SU2C-AACR-DT17-15 (to K.M.S.); and NIH R00CA204602 and DP2CA239597 and the Goldberg-Benioff Endowed Professorship in Prostate Cancer Translational Biology (to L.A.G.). SU2C is a program of the Entertainment Industry Foundation. SU2C research grants are administered by the American Association for Cancer Research, the scientific partner of SU2C.

REFERENCES AND NOTES

- Weinstein IB, Addiction to oncogenes—The Achilles heal of cancer. *Science* 297, 63–64 (2002). [PubMed: 12098689]
- Eifert C, Powers SR, From cancer genomes to oncogenic drivers, tumour dependencies and therapeutic targets. *Nat. Rev. Cancer* 12, 572–578 (2012). [PubMed: 22739505]
- Cox AD, Fesik SW, Kimmelman AC, Luo J, Der CJ, Drugging the undruggable RAS: Mission possible? *Nat. Rev. Drug Discov* 13, 828–851 (2014). [PubMed: 25323927]
- Malumbres M, Barbacid M, RAS oncogenes: The first 30 years. *Nat. Rev. Cancer* 3, 459–465 (2003). [PubMed: 12778136]
- Simanshu DK, Nissley DV, McCormick F, RAS proteins and their regulators in human disease. *Cell* 170, 17–33 (2017). [PubMed: 28666118]
- Downward J, RAS synthetic lethal screens revisited: Still seeking the elusive prize? *Clin. Cancer Res* 21, 1802–1809 (2015). [PubMed: 25878361]
- Aguirre AJ, Hahn WC, Synthetic lethal vulnerabilities in KRAS-mutant cancers. *Cold Spring Harb. Perspect. Med* 8, a031518 (2018).
- Luo J, Emanuele MJ, Li D, Creighton CJ, Schlabach MR, Westbrook TF, Wong KK, Elledge SJ, A genome-wide RNAi screen identifies multiple synthetic lethal interactions with the Ras oncogene. *Cell* 137, 835–848 (2009). [PubMed: 19490893]
- Beronja S, Janki P, Heller E, Lien W-H, Keyes BE, Oshimori N, Fuchs E, RNAi screens in mice identify physiological regulators of oncogenic growth. *Nature* 501, 185–190 (2013). [PubMed: 23945586]
- Kim HS, Mendiratta S, Kim J, Pecot CV, Larsen JE, Zubovych I, Seo BY, Kim J, Eskiocak B, Chung H, McMillan E, Wu S, De Brabander J, Komurov K, Toombs JE, Wei S, Peyton M, Williams N, Gazdar AF, Posner BA, Brekken RA, Sood AK, Deberardinis RJ, Roth MG, Minna

- JD, White MA, Systematic identification of molecular subtype-selective vulnerabilities in non-small-cell lung cancer. *Cell* 155, 552–566 (2013). [PubMed: 24243015]
11. Cullis J, Meiri D, Sandi MJ, Radulovich N, Kent OA, Medrano M, Mokady D, Normand J, Larose J, Marcotte R, Marshall CB, Ikura M, Ketela T, Moffat J, Neel BG, Gingras A-C, Tsao M-S, Rottapel R, The RhoGEF GEF-H1 is required for oncogenic RAS signaling via KSR-1. *Cancer Cell* 25, 181–195 (2014). [PubMed: 24525234]
 12. Wang T, Yu H, Hughes NW, Liu B, Kendirli A, Klein K, Chen WW, Lander ES, Sabatini DM, Gene essentiality profiling reveals gene networks and synthetic lethal interactions with oncogenic Ras. *Cell* 168, 890–903 (2017). [PubMed: 28162770]
 13. Kim J, McMillan E, Kim HS, Venkateswaran N, Makkar G, Rodriguez-Canales J, Villalobos P, Neggers JE, Mendiratta S, Wei S, Landesman Y, Senapedis W, Baloglu E, Chow C-WB, Frink RE, Gao B, Roth M, Minna JD, Daelemans D, Wistuba II, Posner BA, Scaglioni PP, White MA, XPO1-dependent nuclear export is a druggable vulnerability in KRAS-mutant lung cancer. *Nature* 538, 114–117 (2016). [PubMed: 27680702]
 14. Ostrem JM, Peters U, Sos ML, Wells JA, Shokat KM, K-Ras(G12C) inhibitors allosterically control GTP affinity and effector interactions. *Nature* 503, 548–551 (2013). [PubMed: 24256730]
 15. Patricelli MP, Janes MR, Li L-S, Hansen R, Peters U, Kessler LV, Chen Y, Kucharski JM, Feng J, Ely T, Chen JH, Firdaus SJ, Babbar A, Ren P, Liu Y, Selective inhibition of oncogenic KRAS output with small molecules targeting the inactive state. *Cancer Discov* 6, 316–329 (2016). [PubMed: 26739882]
 16. Lito P, Solomon M, Li L-S, Hansen R, Rosen N, Allele-specific inhibitors inactivate mutant KRAS G12C by a trapping mechanism. *Science* 351, 604–608 (2016). [PubMed: 26841430]
 17. Janes MR, Zhang J, Li L-S, Hansen R, Peters U, Guo X, Chen Y, Babbar A, Firdaus SJ, Darjania L, Feng J, Chen JH, Li S, Li S, Long YO, Thach C, Liu Y, Zariw A, Ely T, Kucharski JM, Kessler LV, Wu T, Yu K, Wang Y, Yao Y, Deng X, Zarrinkar PP, Brehmer D, Dhanak D, Lorenzi MV, Hu-Lowe D, Patricelli MP, Ren P, Liu Y, Targeting KRAS mutant cancers with a covalent G12C-specific inhibitor. *Cell* 172, e17, 578–589.e17 (2018). [PubMed: 29373830]
 18. Amgen A phase 1, study evaluating the safety, tolerability, PK, and efficacy of AMG 510 in subjects with solid tumors with a specific KRAS mutation (2018); <https://clinicaltrials.gov/ct2/show/NCT03600883>.
 19. Mirati Therapeutics Inc, MRTX849 in patients with cancer having a KRAS G12C mutation (2018); <https://clinicaltrials.gov/ct2/show/NCT03785249>.
 20. Garraway LA, Jänne PA, Circumventing cancer drug resistance in the era of personalized medicine. *Cancer Discov* 2, 214–226 (2012). [PubMed: 22585993]
 21. Gilbert LA, Horlbeck MA, Adamson B, Villalta JE, Chen Y, Whitehead EH, Guimaraes C, Panning B, Ploegh HL, Bassik MC, Qi LS, Kampmann M, Weissman JS, Genome-scale CRISPR-mediated control of gene repression and activation. *Cell* 159, 647–661 (2014). [PubMed: 25307932]
 22. Horlbeck MA, Gilbert LA, Villalta JE, Adamson B, Pak RA, Chen Y, Fields AP, Park CY, Corn JE, Kampmann M, Weissman JS, Compact and highly active next-generation libraries for CRISPR-mediated gene repression and activation. *eLife* 5, e19760 (2016).
 23. Lenoir WF, Lim TL, Hart T, PICKLES: The database of pooled in-vitro CRISPR knockout library essentiality screens. *Nucleic Acids Res* 46, D776–D780 (2018). [PubMed: 29077937]
 24. Meyers RM, Bryan JG, McFarland JM, Weir BA, Sizemore AE, Xu H, Dharia NV, Montgomery PG, Cowley GS, Pantel S, Goodale A, Lee Y, Ali LD, Jiang G, Lubonja R, Harrington WF, Strickland M, Wu T, Hawes DC, Zhivich VA, Wyatt MR, Kalani Z, Chang JJ, Okamoto M, Stegmaier K, Golub TR, Boehm JS, Vazquez F, Root DE, Hahn WC, Tsherniak A, Computational correction of copy number effect improves specificity of CRISPR–Cas9 essentiality screens in cancer cells. *Nat. Genet* 49, 1779–1784 (2017). [PubMed: 29083409]
 25. Jiang H, Pritchard JR, Williams RT, Lauffenburger DA, Hemann MT, A mammalian functional-genetic approach to characterizing cancer therapeutics. *Nat. Chem. Biol* 7, 92–100 (2010). [PubMed: 21186347]
 26. Vallejo A, Perurena N, Guruceaga E, Mazur PK, Martinez-Canarias S, Zandueta C, Valencia K, Arricibita A, Gwinn D, Sayles LC, Chuang C-H, Guembe L, Bailey P, Chang DK, Biankin A, Ponz-Sarvise M, Andersen JB, Khatri P, Bozec A, Sweet-Cordero EA, Sage J, Lecanda F, Vicent

- S, An integrative approach unveils FOSL1 as an oncogene vulnerability in KRAS-driven lung and pancreatic cancer. *Nat. Commun* 8, 14294 (2017). [PubMed: 28220783]
27. Sunaga N, Shames DS, Girard L, Peyton M, Larsen JE, Imai H, Soh J, Sato M, Yanagitani N, Kaira K, Xie Y, Gazdar AF, Mori M, Minna JD, Knockdown of oncogenic KRAS in non-small cell lung cancers suppresses tumor growth and sensitizes tumor cells to targeted therapy. *Mol. Cancer Ther* 10, 336–346 (2011). [PubMed: 21306997]
 28. Misale S, Fatherree JP, Cortez E, Li C, Bilton S, Timonina D, Myers DT, Lee D, Gomez-Caraballo M, Greenberg M, Nangia V, Greninger P, Egan RK, McClanaghan J, Stein GT, Murchie E, Zarrinkar PP, Janes MR, Li L-S, Liu Y, Hata AN, Benes CH, KRAS G12C NSCLC models are sensitive to direct targeting of KRAS in combination with PI3K inhibition. *Clin. Cancer Res* 25, 796–807 (2019). [PubMed: 30327306]
 29. Lemmon MA, Schlessinger J, Cell signaling by receptor tyrosine kinases. *Cell* 141, 1117–1134 (2010). [PubMed: 20602996]
 30. Barretina J, Caponigro G, Stransky N, Venkatesan K, Margolin AA, Kim S, Wilson CJ, Lehár J, Kryukov GV, Sonkin D, Reddy A, Liu M, Murray L, Berger MF, Monahan JE, Morais P, Meltzer J, Korejwa A, Jané-Valbuena J, Mapa FA, Thibault J, Bric-Furlong E, Raman P, Shipway A, Engels IH, Cheng J, Yu GK, Yu J, Aspesi P Jr., de Silva M, Jagtap K, Jones MD, Wang L, Hatton C, Palescandolo E, Gupta S, Mahan S, Sougnez C, Onofrio RC, Liefeld T, MacConaill L, Winckler W, Reich M, Li N, Mesirov JP, Gabriel SB, Getz G, Ardlie K, Chan V, Myer VE, Weber BL, Porter J, Warmuth M, Finan P, Harris JL, Meyerson M, Golub TR, Morrissey MP, Sellers WR, Schlegel R, Garraway LA, The Cancer Cell Line Encyclopedia enables predictive modelling of anticancer drug sensitivity. *Nature* 483, 603–607 (2012). [PubMed: 22460905]
 31. Eser S, Schnieke A, Schneider G, Saur D, Oncogenic KRAS signalling in pancreatic cancer. *Br. J. Cancer* 111, 817–822 (2014). [PubMed: 24755884]
 32. Román M, Baraibar I, López I, Nadal E, Rolfo C, Vicent S, Gil-Bazo I, KRAS oncogene in non-small cell lung cancer: Clinical perspectives on the treatment of an old target. *Mol. Cancer* 17, 33 (2018). [PubMed: 29455666]
 33. Zeng M, Lu J, Li L, Feru F, Quan C, Gero TW, Ficarro SB, Xiong Y, Ambrogio C, Paranal RM, Catalano M, Shao J, Wong K-K, Marto JA, Fischer ES, Jänne PA, Scott DA, Westover KD, Gray NS, Potent and selective covalent quinazoline inhibitors of KRAS G12C. *Cell Chem. Biol* 24, 1005–1016.e3 (2017). [PubMed: 28781124]
 34. Tape CJ, Ling S, Dimitriadi M, McMahon KM, Worboys JD, Leong HS, Norrie IC, Miller CJ, Poulgiannis G, Lauffenburger DA, Jørgensen C, Oncogenic KRAS regulates tumor cell signaling via stromal reciprocation. *Cell* 165, 910–920 (2016). [PubMed: 27087446]
 35. Kelsey I, Manning BD, mTORC1 status dictates tumor response to targeted therapeutics. *Sci. Signal* 6, pe31 (2013).
 36. Vartanian S, Bentley C, Brauer MJ, Li L, Shirasawa S, Sasazuki T, Kim J-S, Haverty P, Stawiski E, Modrusan Z, Waldman T, Stokoe D, Identification of mutant K-Ras-dependent phenotypes using a panel of isogenic cell lines. *J. Biol. Chem* 288, 2403–2413 (2013). [PubMed: 23188824]
 37. Fujita-Sato S, Galeas J, Truitt M, Pitt C, Urisman A, Bandyopadhyay S, Ruggero D, McCormick F, Enhanced MET translation and signaling sustains K-Ras-driven proliferation under anchorage-independent growth conditions. *Cancer Res* 75, 2851–2862 (2015). [PubMed: 25977330]
 38. Chou T-C, Drug combination studies and their synergy quantification using the Chou-Talalay method. *Cancer Res* 70, 440–446 (2010). [PubMed: 20068163]
 39. Sherr CJ, Principles of tumor suppression. *Cell* 116, 235–246 (2004). [PubMed: 14744434]
 40. Puyol M, Martín A, Dubus P, Mulero F, Pizcueta P, Khan G, Guerra C, Santamaría D, Barbacid M, A synthetic lethal interaction between K-Ras oncogenes and Cdk4 unveils a therapeutic strategy for non-small cell lung carcinoma. *Cancer Cell* 18, 63–73 (2010). [PubMed: 20609353]
 41. Eli Lilly A study of abemaciclib (LY2835219) in participants with previously treated KRAS mutated lung cancer (JUNIPER) (2014); <https://clinicaltrials.gov/ct2/show/NCT02152631>.
 42. Huang da W, Sherman BT, Lempicki RA, Systematic and integrative analysis of large gene lists using DAVID bioinformatics resources. *Nat. Protoc* 4, 44–57 (2009). [PubMed: 19131956]
 43. Ruess DA, Heynen GJ, Ciecieski KJ, Ai J, Berninger A, Kabacaoglu D, Görgülü K, Dantes Z, Wörmann SM, Diakopoulos KN, Karpathaki AF, Kowalska M, Kaya-Aksoy E, Song L, van der

- Laan EAZ, López-Alberca MP, Nazaré M, Reichert M, Saur D, Erkan MM, Hopt UT, Sainz B Jr., Birchmeier W, Schmid RM, Lesina M, Algül H, Mutant KRAS-driven cancers depend on PTPN11/SHP2 phosphatase. *Nat. Med* 24, 954–960 (2018). [PubMed: 29808009]
44. Mainardi S, Mulero-Sánchez A, Prahallad A, Germano G, Bosma A, Krimpenfort P, Lieftink C, Steinberg JD, de Wit N, Gonçalves-Ribeiro S, Nadal E, Bardelli A, Villanueva A, Bernards R, SHP2 is required for growth of KRAS-mutant non-small-cell lung cancer in vivo. *Nat. Med* 24, 961–967 (2018). [PubMed: 29808006]
45. Kruspig B, Monteverde T, Neidler S, Hock A, Kerr E, Nixon C, Clark W, Hedley A, Laing S, Coffelt SB, Quesne J. Le, Dick C, Vousden KH, Martins CP, Murphy DJ, The ERBB network facilitates KRAS-driven lung tumorigenesis. *Sci. Transl. Med* 10, eaao2565 (2018).
46. Moll HP, Pranz K, Musteanu M, Grabner B, Hruschka N, Mohrherr J, Aigner P, Stiedl P, Brcic L, Laszlo V, Schramek D, Moriggl R, Eferl R, Moldvay J, Dezso K, Lopez-Casas PP, Stoiber D, Hidalgo M, Penninger J, Sibilia M, Győrffy B, Barbacid M, Dome B, Popper H, Casanova E, Afatinib restrains K-RAS-driven lung tumorigenesis. *Sci. Transl. Med* 10, eaao2301 (2018).
47. Nichols RJ, Haderk F, Stahlhut C, Schulze CJ, Hemmati G, Wildes D, Tzitzilonis C, Mordec K, Marquez A, Romero J, Hsieh T, Zaman A, Olivás V, McCoach C, Blakely CM, Wang Z, Kiss G, Koltun ES, Gill AL, Singh M, Goldsmith MA, Smith JAM, Bivona TG, RAS nucleotide cycling underlies the SHP2 phosphatase dependence of mutant BRAF-, NF1- and RAS-driven cancers. *Nat. Cell Biol* 20, 1064–1073 (2018). [PubMed: 30104724]
48. Smalley KSM, Lioni M, Palma M, Dalla, Xiao M, Desai B, Egyhazi S, Hansson J, Wu H, King AJ, Van Belle P, Elder DE, Flaherty KT, Herlyn M, Nathanson KL, Increased cyclin D1 expression can mediate BRAF inhibitor resistance in BRAF V600E-mutated melanomas. *Mol. Cancer Ther* 7, 2876–2883 (2008). [PubMed: 18790768]
49. Blakely CM, Watkins TBK, Wu W, Gini B, Chabon JJ, McCoach CE, McGranahan N, Wilson GA, Birkbak NJ, Olivás VR, Rotow J, Maynard A, Wang V, Gubens MA, Banks KC, Lanman RB, Caulin AF, St John J, Cordero AR, Giannikopoulos P, Simmons AD, Mack PC, Gandara DR, Husain H, Doebele RC, Riess JW, Diehn M, Swanton C, Bivona TG, Evolution and clinical impact of co-occurring genetic alterations in advanced-stage EGFR-mutant lung cancers. *Nat. Genet* 49, 1693–1704 (2017). [PubMed: 29106415]
50. Roskoski R Jr., Classification of small molecule protein kinase inhibitors based upon the structures of their drug-enzyme complexes. *Pharmacol. Res* 103, 26–48 (2016). [PubMed: 26529477]
51. Novotny CJ, Pollari S, Park JH, Lemmon MA, Shen W, Shokat KM, Overcoming resistance to HER2 inhibitors through state-specific kinase binding. *Nat. Chem. Biol* 12, 923–930 (2016). [PubMed: 27595329]
52. Li S, Liu S, Deng J, Akbay EA, Hai J, Ambrogio C, Zhang L, Zhou F, Jenkins RW, Adeegbe DO, Gao P, Wang X, Paweletz CP, Herter-Sprie GS, Chen T, Gutiérrez-Quiceno L, Zhang Y, Merlino AA, Quinn MM, Zeng Y, Yu X, Liu Y, Fan L, Aguirre AJ, Barbie DA, Yi X, Wong K-K, Assessing therapeutic efficacy of MEK inhibition in a KRASG12C-driven mouse model of lung cancer. *Clin. Cancer Res* 24, 4854–4864 (2018). [PubMed: 29945997]
53. Lee MJ, Ye AS, Gardino AK, Heijink AM, Sorger PK, MacBeath G, Yaffe MB, Sequential application of anticancer drugs enhances cell death by rewiring apoptotic signaling networks. *Cell* 149, 780–794 (2012). [PubMed: 22579283]
54. Hart T, Moffat J, BAGEL: A computational framework for identifying essential genes from pooled library screens. *BMC Bioinf* 17, 164 (2016).
55. Beltrao P, Albanèse V, Kenner LR, Swaney DL, Burlingame A, Villén J, Lim WA, Fraser JS, Frydman J, Krogan NJ, Systematic functional prioritization of protein posttranslational modifications. *Cell* 150, 413–425 (2012). [PubMed: 22817900]
56. Cox J, Mann M, MaxQuant enables high peptide identification rates, individualized p.p.b.-range mass accuracies and proteome-wide protein quantification. *Nat. Biotechnol* 26, 1367–1372 (2008). [PubMed: 19029910]
57. Choi M, Chang C-Y, Clough T, Broudy D, Killeen T, MacLean B, Vitek O, MSstats: An R package for statistical analysis of quantitative mass spectrometry-based proteomic experiments. *Bioinformatics* 30, 2524–2526 (2014). [PubMed: 24794931]
58. Hu J, Rho H-S, Newman RH, Zhang J, Zhu H, Qian J, PhosphoNetworks: A database for human phosphorylation networks. *Bioinformatics* 30, 141–142 (2013). [PubMed: 24227675]

59. Huang K-Y, Wu H-Y, Chen Y-J, Lu C-T, Su M-G, Hsieh Y-C, Tsai C-M, Lin K-I, Huang H-D, Lee T-Y, Chen Y-J, RegPhos 2.0: An updated resource to explore protein kinase–substrate phosphorylation networks in mammals. Database 2014, bau034 (2014).
60. Love M, Huber W, Anders S, Moderated estimation of fold change and dispersion for RNA-seq data with DESeq2. Genome Biol 15, 550 (2014). [PubMed: 25516281]
61. Morton CL, Houghton PJ, Establishment of human tumor xenografts in immunodeficient mice. Nat. Protoc 2, 247–250 (2007). [PubMed: 17406581]

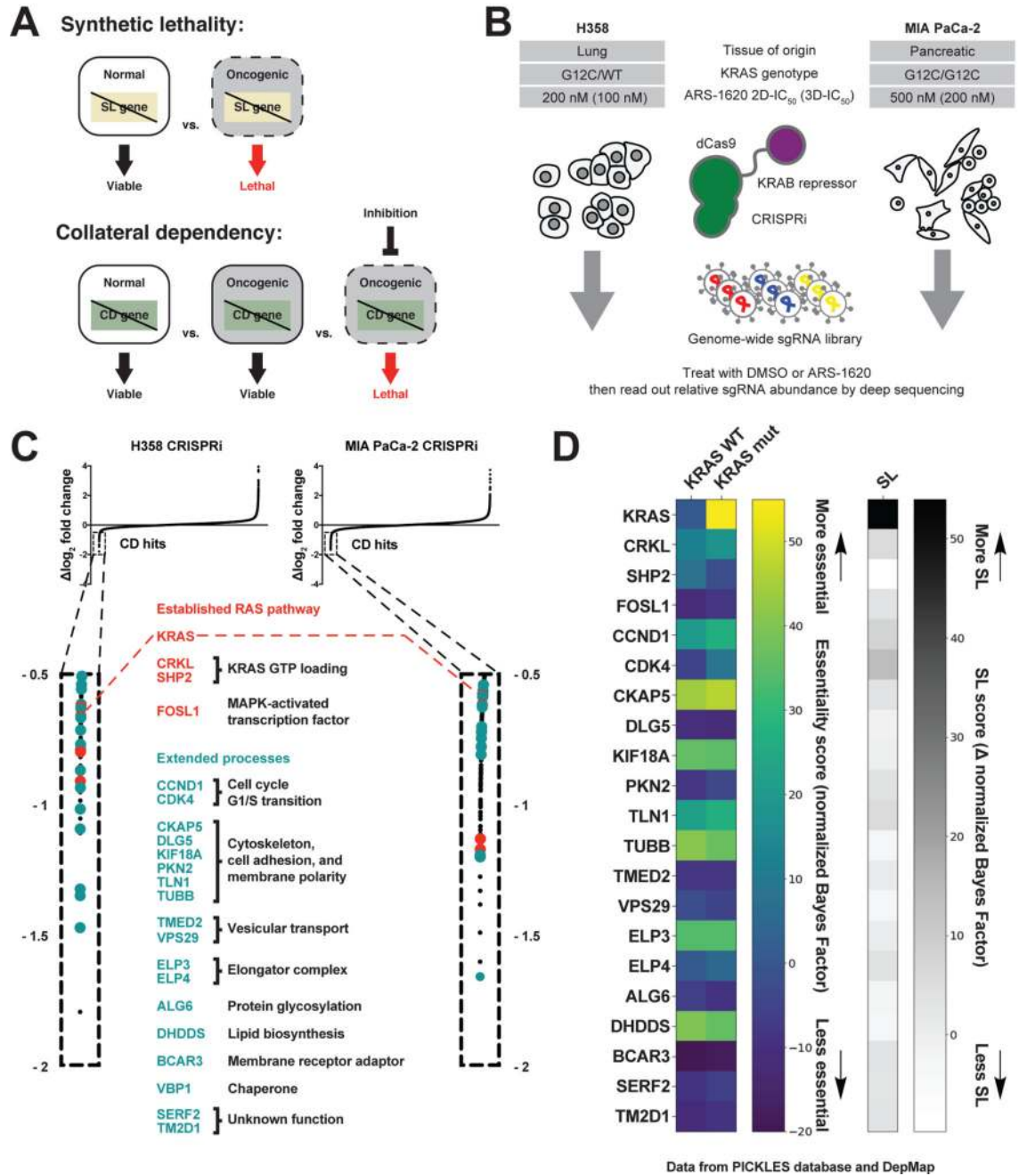


Fig. 1. Genome-scale CRISPRi screens reveal overlapping CDs that govern the cellular impact of direct KRAS^{G12C} inhibition.

(A) Graphic delineating the concepts of SL and CD. (B) Schematic of cancer cell line selection criteria and genome-wide CRISPRi-based screening strategy for CDs. (C) Gene phenotypes from ARS-1620 CRISPRi screens in H358 and MIA PaCa-2 cells. Overlapping collateral dependent genes (hits determined by $\Delta\log_2$ fold change < -0.5) that sensitize to KRAS^{G12C} inhibition are highlighted and functionally categorized: established RAS pathway (red) and extended processes (teal). Cells were grown in 2D adherent culture. Data

represent two biological replicates. **(D)** Average essentiality scores (normalized Bayes factors) of hit CDs were determined by combining data from publicly available resources (PICKLES database and DepMap) for all available KRAS-WT and KRAS-mutant NSCLC cell lines. Color intensities portray higher (yellow) or lower (blue) essentiality scores. Grayscale intensities portray higher (black) or lower (white) SL scores, calculated by subtracting KRAS-WT from KRAS-mutant average essentiality scores.

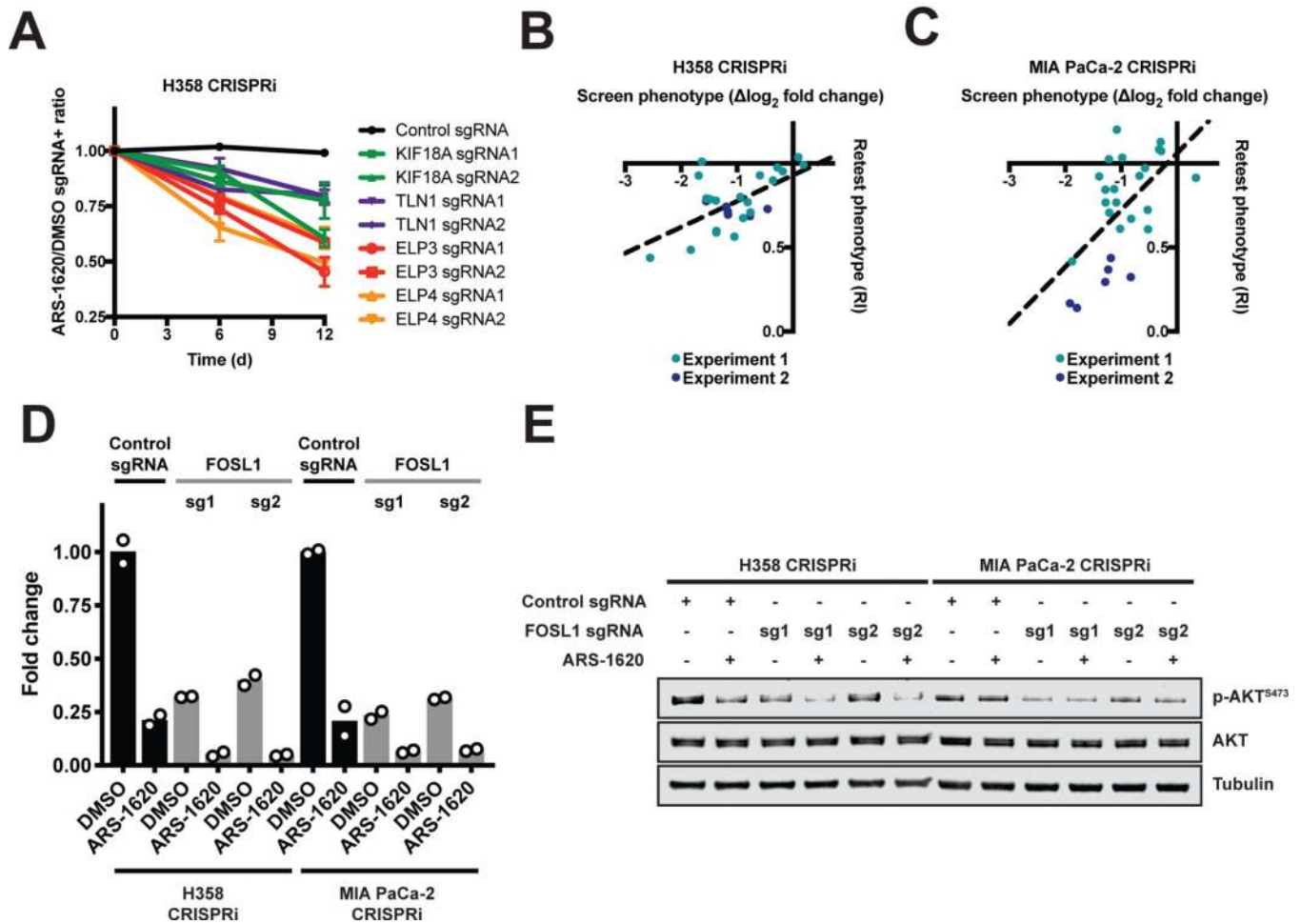


Fig. 2. KRAS^{G12C} inhibition selectively potentiates the essentiality of collateral dependent genes. (A) H358 CRISPRi cells transduced with a negative control sgRNA or each of two sgRNAs targeting the indicated genes were grown in the presence or absence of ARS-1620 (300 nM) in a mixed population growth assay. Relative populations of sgRNA-expressing (fluorescent-positive) or non-sgRNA-expressing (fluorescent-negative) cells were determined by flow cytometry for the times shown. Cells were grown in 2D adherent culture. Data represent an initial value (day 0) as well as means of two biological replicates (days 6 and 12); error bars denote standard deviation (SD). (B) Correlation plot comparing screen phenotypes ($\Delta\log_2$ fold change) to retest phenotypes (RI) in H358 CRISPRi cells. Retest phenotypes were determined from the endpoints of experiments as in (A). Points represent individual sgRNAs. Cells were treated with 300 nM ARS-1620 in experiment 1 (teal) and 1 μ M ARS-1620 in experiment 2 (blue). Cells were grown in 2D adherent culture. $\Delta\log_2$ fold change and RI represent means of two biological replicates. (C) As in (B) in MIA PaCa-2 CRISPRi cells treated with 300 nM (experiment 1, teal) and 3.3 μ M ARS-1620 (experiment 2, blue). (D) RT-qPCR in H358 CRISPRi and MIA PaCa-2 CRISPRi cells transduced with a negative control sgRNA or sgRNAs targeting *FOSL1* and then treated with DMSO or ARS-1620 (1 μ M) for 24 hours. Cells were grown in 3D spheroid culture. Data represent

means of two biological replicates. **(E)** Immunoblots of H358 and MIA PaCa-2 cells as in **(D)**. Cells were grown in 3D spheroid culture. Immunoblots are representative of two biological replicates (see also fig. S3).

Author Manuscript

Author Manuscript

Author Manuscript

Author Manuscript

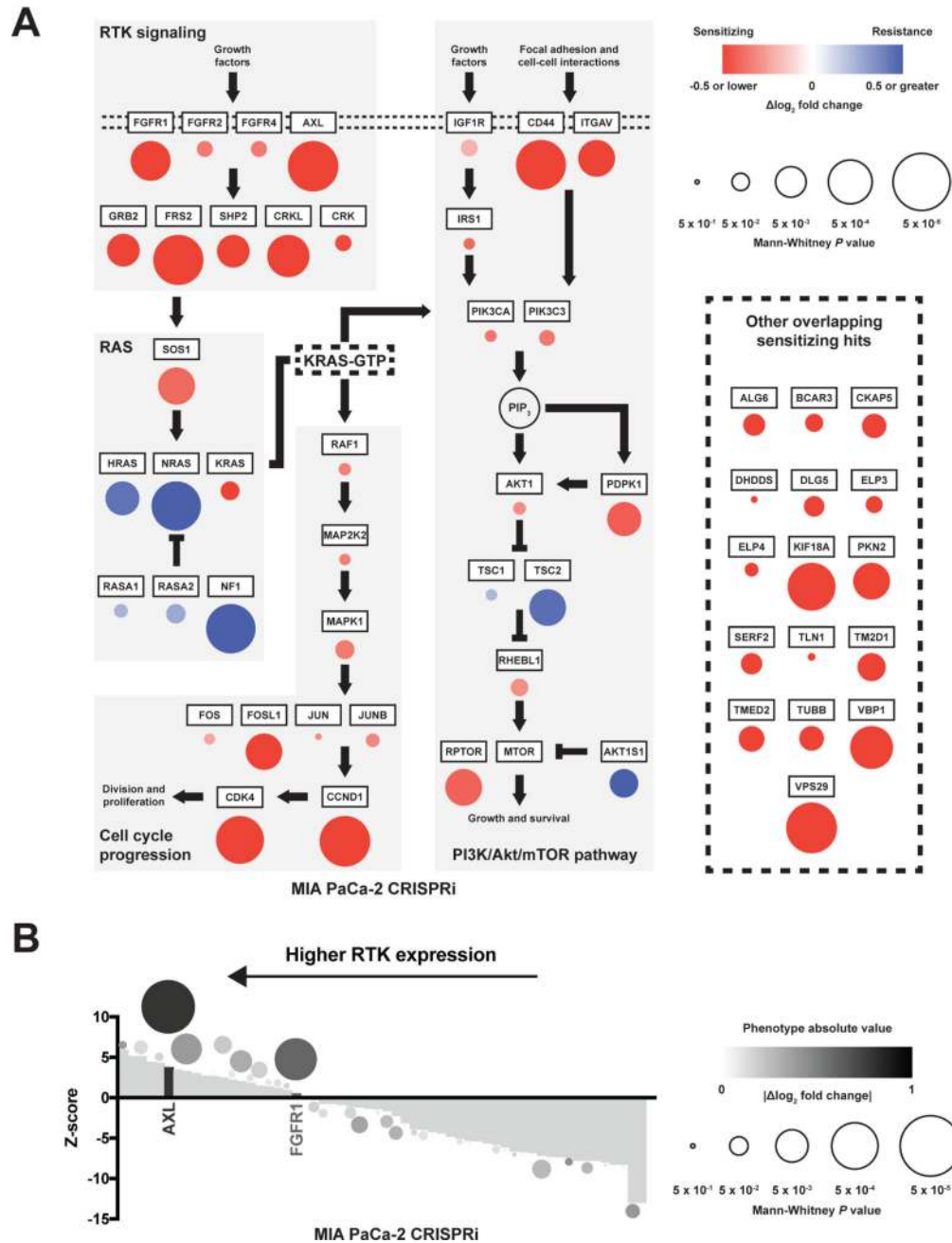


Fig. 3. Critical signaling modules cooperatively sustain a KRAS^{G12C}-driven pro-growth and pro-survival program around KRAS-GTP.
(A) Pathway map of CRISPRi screen gene phenotypes and Mann-Whitney *P* values from MIA PaCa-2 ARS-1620 sensitization (red) and resistance (blue). Color intensities portray phenotype strength, and circle diameters represent $-\log_{10}$ Mann-Whitney *P* values derived from the CRISPRi screen. **(B)** Waterfall plot of expression data from the Cancer Cell Line Encyclopedia (CCLE) and phenotype magnitudes of 58 human RTKs from the CRISPRi screen in MIA PaCa-2 cells. *Z* score on the *x* axis represents normalized mRNA expression

data from RNA-seq, whereas color intensity and circle size represent phenotypes and Mann-Whitney P values from the CRISPRi screen, respectively. Cells in (A) and (B) were grown in 2D adherent culture. Phenotypes in (A) and (B) represent two biological replicates.

Author Manuscript

Author Manuscript

Author Manuscript

Author Manuscript

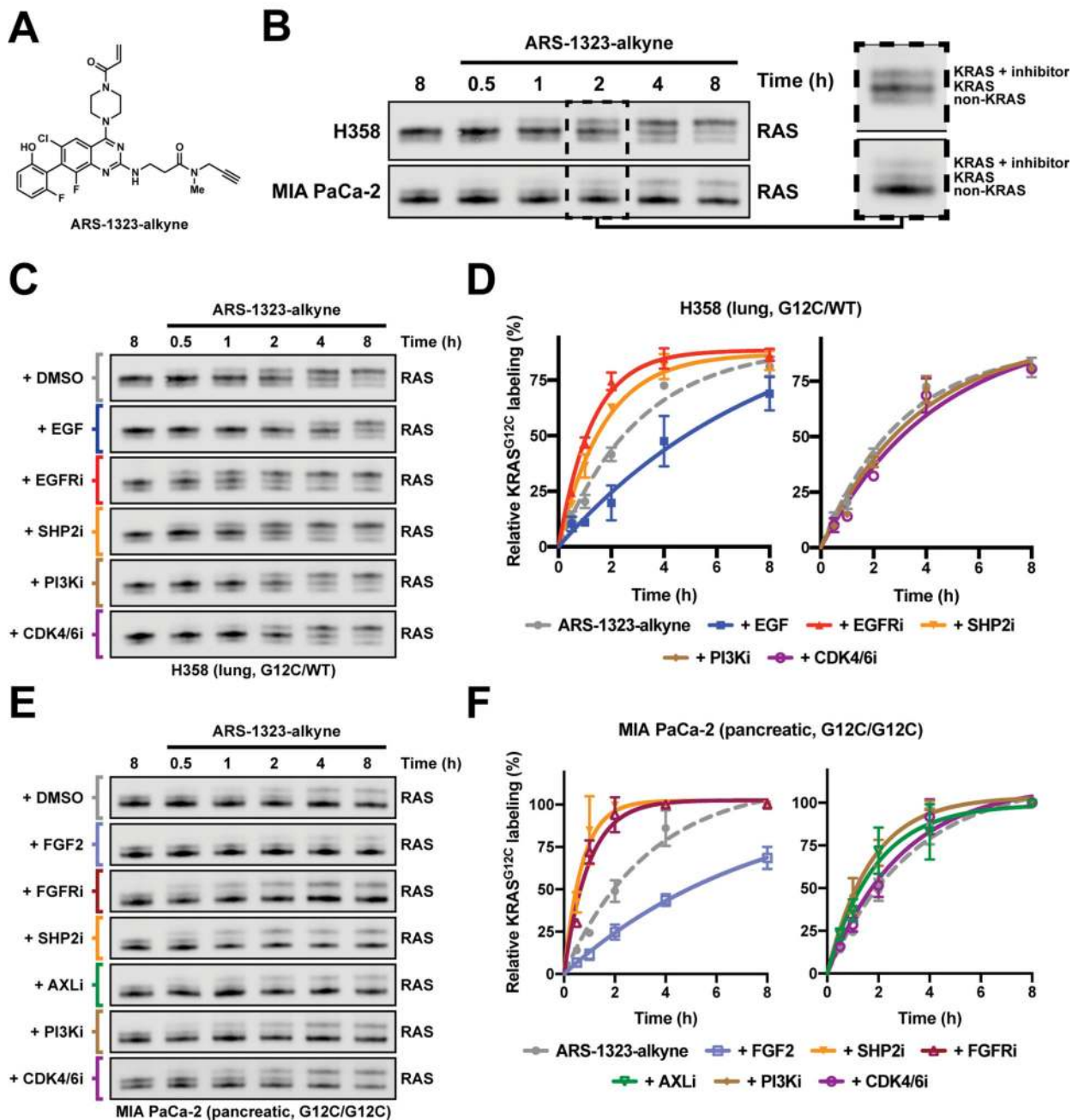
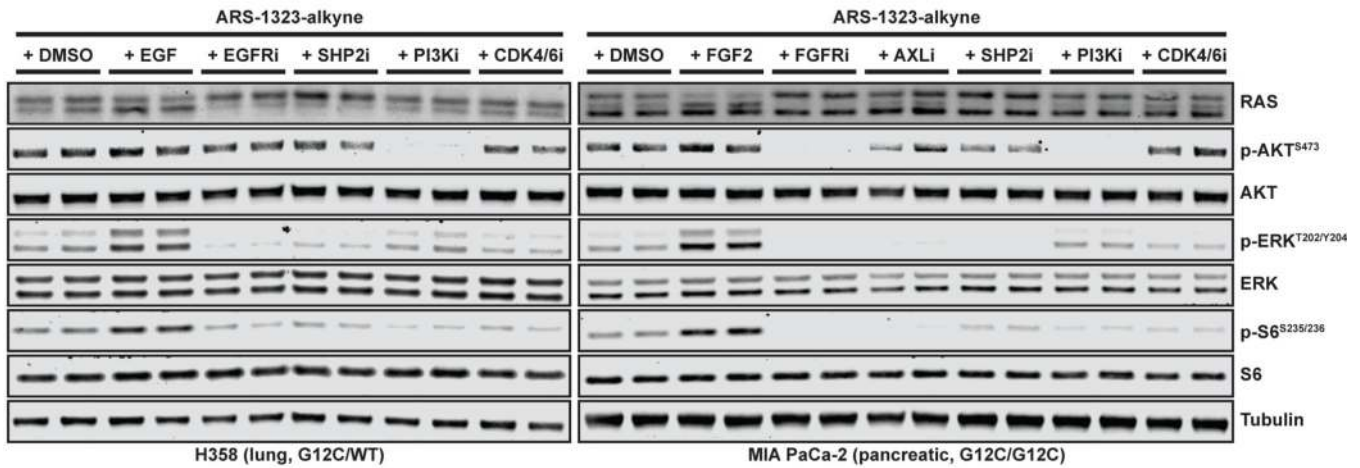


Fig. 4. Combination therapies targeting CD4s with KRAS^{G12C} differ in their ability to promote S-IIP target engagement.

(A) Chemical structure of the KRAS^{G12C} occupancy probe ARS-1323-alkyne. (B) Magnified immunoblots indicating the identities of different bands resulting from electromobility shift after treatment of H358 and MIA PaCa-2 cells with ARS-1323-alkyne (10 μM) and copper-catalyzed click reaction of lysate with TAMRA-N₃. (C and D) Representative immunoblots (C) and relative densitometry of upper (KRAS + inhibitor) and lower (KRAS) bands (D) of H358 cells treated with ARS-1323-alkyne (10 μM)

simultaneously with DMSO [same as shown in (B) to facilitate comparison], EGF (100 ng/ml), erlotinib (10 μ M, EGFRi), SHP099 (10 μ M, SHP2i), buparlisib (10 μ M, PI3Ki), or palbociclib (10 μ M, CDK4/6i) for the times indicated. Lysates were subjected to copper-catalyzed click reaction with TAMRA-N₃. Relative densitometry was quantified using upper (KRAS + inhibitor) and lower (KRAS) bands. (E and F) As in (C) and (D), respectively, for MIA PaCa-2 cells. Instead of EGF and erlotinib, MIA PaCa-2 cells were treated with FGF2 (100 ng/ml), AZD4547 (10 μ M, FGFRi), and bemcentinib (10 μ M, AXLi). Other compounds were administered at the same dose as indicated in (C). Cells in (B) to (F) were grown in 3D spheroid culture. Immunoblots in (B), (C), and (E) are representative of three biological replicates. Data in (D) and (F) represent means of three biological replicates; error bars denote SD.

A



B

| | RTKs and RTK adaptors | | | | PI3K/Akt/mTOR pathway | Cell cycle progression |
|------------|-----------------------|-------|------|-------|-----------------------|------------------------|
| | EGFRi | FGFRi | AXLi | SHP2i | PI3Ki | CDK4/6i |
| H358 | 0.28 | 0.70 | 0.97 | 0.40 | 0.67 | 0.56 |
| MIA PaCa-2 | * | 0.27 | 0.40 | 0.33 | 0.28 | 0.34 |
| H23 | 0.79 | 0.64 | 1.23 | 0.32 | 0.45 | 0.42 |

Chou-Talalay Combination Index (CI)
 Synergy (CI < 0.75), Additivity (0.75 < CI < 1.25), Antagonism (CI > 1.25)
 *IC₅₀ not reached for EGFRi

C

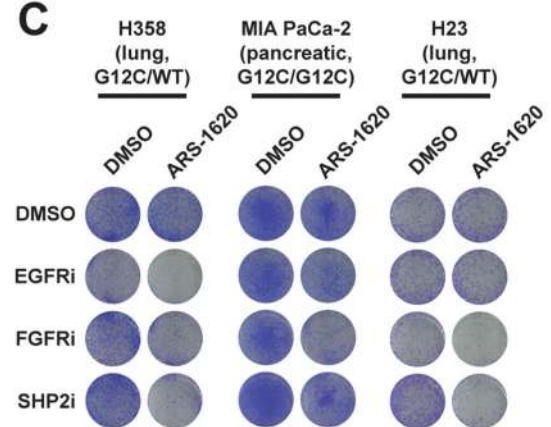


Fig. 5. CDIs with KRAS^{G12C} cooperatively sustain downstream signaling outputs to promote survival and proliferation.

(A) Immunoblots of H358 and MIA PaCa-2 cells treated with ARS-1323-alkyne (10 μ M) simultaneously with DMSO, EGF (100 ng/ml), FGF2 (100 ng/ml), erlotinib (10 μ M, EGFRi), AZD4547 (10 μ M, FGFRi), bemcentinib (10 μ M, AXLi), SHP099 (10 μ M, SHP2i), buparlisib (10 μ M, PI3Ki), or palbociclib (10 μ M, CDK4/6i) for 2 hours. Lysates were subjected to copper-catalyzed click reaction with TAMRA-N₃. Cells were grown in 3D spheroid culture. Immunoblots represent two biological replicates. (B) Combination indices (CIs) derived from drug synergism in three KRAS^{G12C}-mutant cell lines assessed in 3D spheroid culture. Cell viability was determined after 5-day treatment with ARS-1620, second compounds, or the combination in a 1:1 ratio (dilution series from 1.5 nM to 10 μ M), and CI values were calculated using CompuSyn 1.0 from three biological replicates. CI < 0.75 indicates synergism with ARS-1620 (red), CI = 0.75 to 1.25 indicates additivity, and CI > 1.25 indicates antagonism. (C) Clonogenic assays of three KRAS^{G12C}-mutant cell lines cultured with indicated compounds or combinations thereof in 2D adherent culture. H358 (300 nM), MIA PaCa-2 (1 μ M), and H23 (1 μ M) cells were treated using ARS-1620 and

second compounds at a 1:1 concentration. Data are representative of three biological replicates.

Author Manuscript

Author Manuscript

Author Manuscript

Author Manuscript

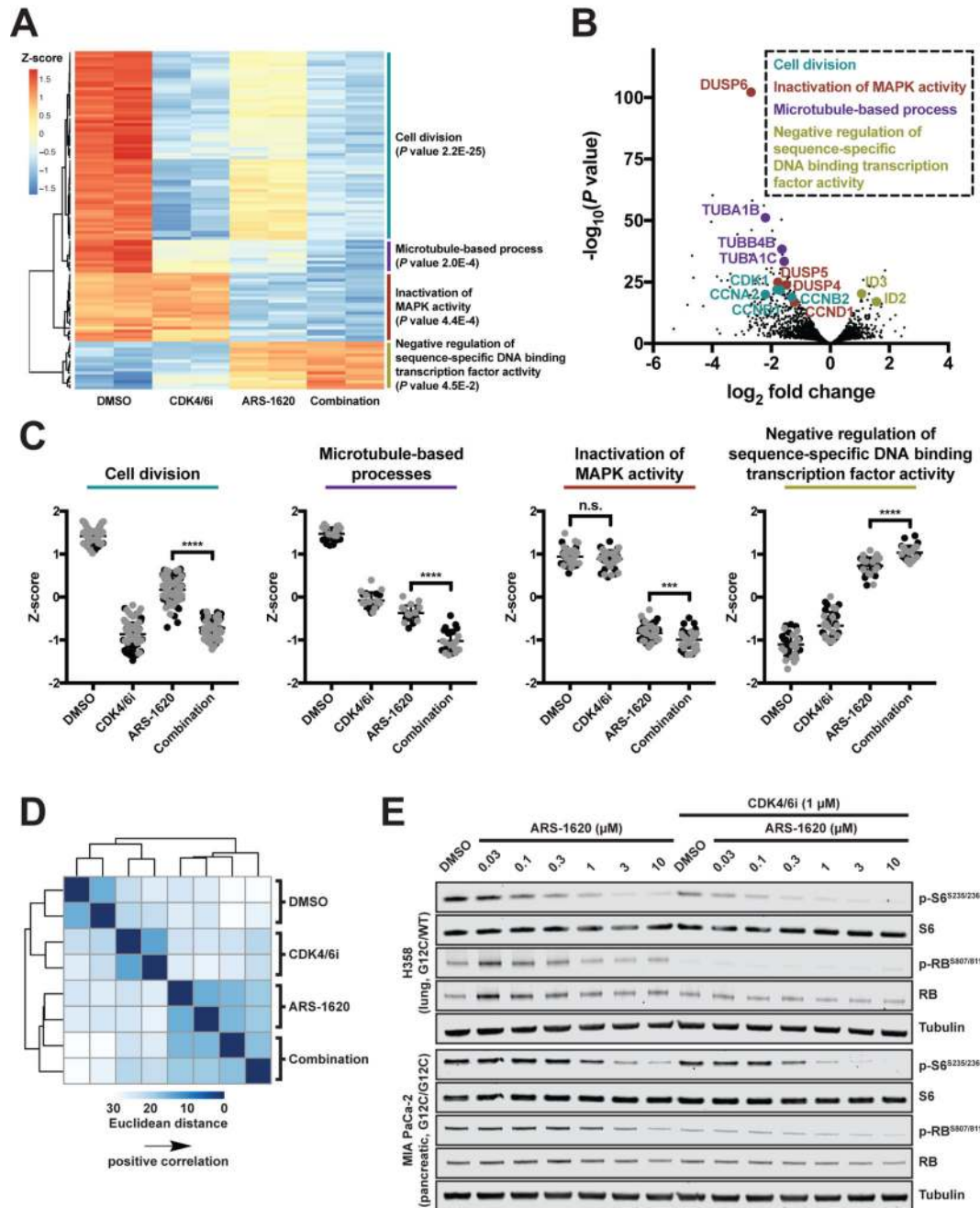


Fig. 6. CDK4/6 coinhibition enhances global antiproliferative effects of KRAS^{G12C} inhibition. (A) Heatmap displaying top significant (adjusted $P < 5 \times 10^{-14}$ by a Wald test) differentially expressed genes in H358 cells between DMSO and combination treatments, hierarchically clustered based on Pearson correlation distances. Gene expression values were Z score–normalized to the average expression value of each row. Total RNA was isolated following 24-hour treatment with DMSO, palbociclib (1 μM , CDK4/6i), ARS-1620 (1 μM), or their combination in H358 cells. Gene ontology enrichment terms for four major clusters are indicated. Data represent two biological replicates. (B) Volcano plot of \log_2 fold changes

and P values from the experiment in (A). (C) Statistical analysis of differences in gene expression among clusters shown in (A). Data points represent individual genes. Biological replicates are shown as black and gray points. *** $P < 0.001$, **** $P < 0.0001$ by an unpaired t test. n.s., not significant. (D) Pairwise correlation matrix from the experiment in (A) between treatment conditions displaying global similarities in expression profiles based on Euclidean distances. (E) Immunoblots of H358 or MIA PaCa-2 cells cotreated with a dose range of ARS-1620 with DMSO or palbociclib (1 μ M, CDK4/6i) for 24 hours. Cells in (A) to (E) were grown in 3D spheroid culture. Immunoblots are representative of two biological replicates (see also fig. S6).

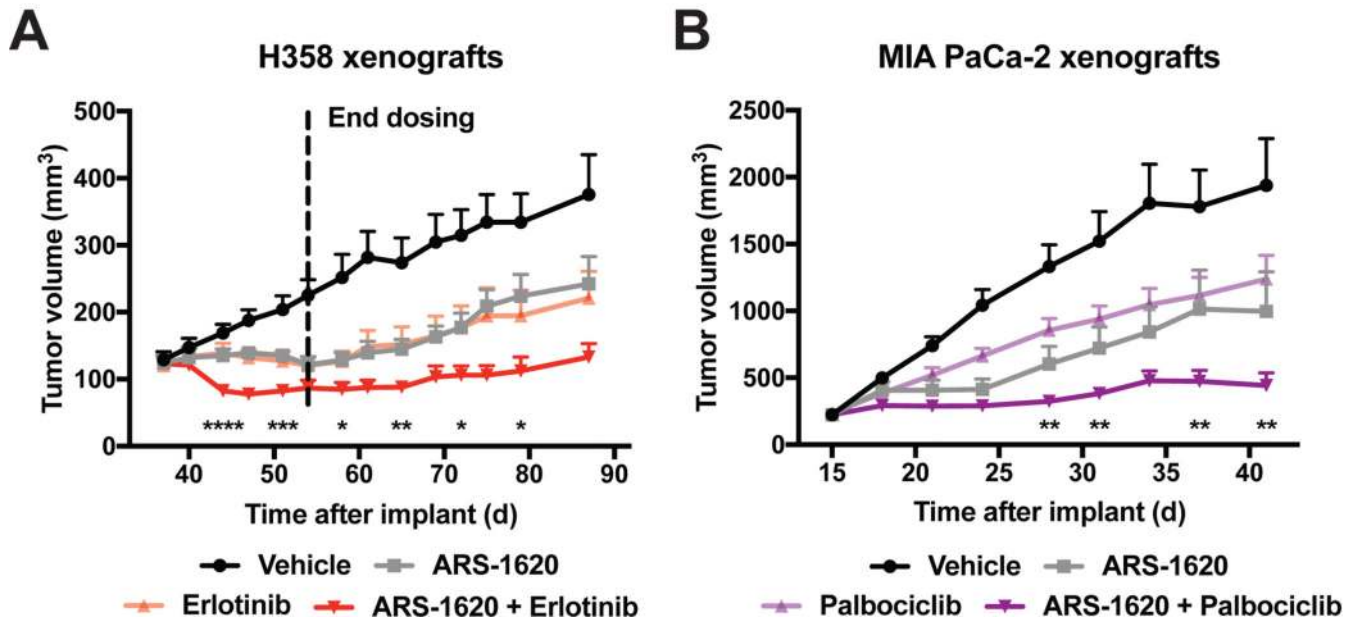


Fig. 7. Pharmacological targeting of CD4 promotes response to KRAS^{G12C} inhibition in vivo. (A) Tumor volumes in mice bearing H358 xenografts and treated with vehicle, ARS-1620 (100 mg/kg), erlotinib (80 to 100 mg/kg, EGFRi), or their combination. Treatment was stopped 54 days after initial implantation to monitor the durability of observed responses. $n \geq 4$ mice per group; error bars denote SEM. * $P < 0.05$, ** $P < 0.01$, *** $P < 0.001$, **** $P < 0.0001$ comparing ARS-1620 and combination arms by a Mann-Whitney test. (B) Tumor volumes in mice bearing MIA PaCa-2 xenografts and treated with vehicle, ARS-1620 (100 mg/kg), palbociclib (100 mg/kg, CDK4/6i), or their combination. $n \geq 8$ mice per group; error bars denote SEM. * $P < 0.05$, ** $P < 0.01$, *** $P < 0.001$, **** $P < 0.0001$ comparing ARS-1620 and combination arms by a Mann-Whitney test.